Article:
Childerhouse, T. orcid.org/0000-0001-9669-3806, M'Saoubi, R., Franca, L. et al. (3 more authors) (2022) The influence of machining induced surface integrity and residual stress on the fatigue performance of Ti-6Al-4V following polycrystalline diamond and coated cemented carbide milling. International Journal of Fatigue, 163. 107054. ISSN 0142-1123

https://doi.org/10.1016/j.ijfatigue.2022.107054

International Journal of Fatigue 163 (2022) 107054

Contents lists available at ScienceDirect

International Journal of Fatigue

journal homepage: www.elsevier.com/locate/ijfatigue

The influence of machining induced surface integrity and residual stress on the fatigue performance of Ti-6Al-4V following polycrystalline diamond and coated cemented carbide milling

Thomas Childerhouse [a,e,*], Rachid M'Saoubi [b,c], Luiz Franca [d], Nick Weston [a], Pete Crawforth [e], Martin Jackson [a]

[a] Department of Materials Science and Engineering, University of Sheffield, Sir Robert Hadfield Building, Mappin Street, Sheffield, S1 3JD, UK
[b] Materials & Technology Development, Seco Tools AB, SE73782, Fagersta, Sweden
[c] Department of Mechanical Engineering Sciences, Division of Production and Materials Engineering, Lund University, Naturvetarvägen 18, 223 62 Lund, Sweden
[d] Element Six Global Innovation Centre, Fermi Avenue, Harwell, OX11 0QR, UK
[e] Advanced Manufacturing Research Centre with Boeing, University of Sheffield, Rotherham, S60 5TZ, UK

ARTICLE INFO

Keywords:
Finish machining
Crack initiation and growth
Tool wear
Titanium alloys
Powder metallurgy

ABSTRACT

Accurate fatigue life predictions of titanium alloy components requires an understanding of how the machining affected metallurgical and micro-mechanical subsurface condition influences fatigue crack nucleation and growth. This study investigates the influence of surface integrity features generated during carbide and high-speed polycrystalline diamond machining on the fatigue behaviour of coarse and fine-grained Ti-6Al-4V. Mechanically induced compressive residual stresses, promoted by higher feed rates and the larger cutting edge radii of carbide tools, have been demonstrated to provide an overriding enhancing effect on fatigue life due to crack initiation suppression and reducing the deleterious effects of microstructural deformation and surface imperfections.

1. Introduction

The machining induced surface integrity of titanium alloy components plays a critical role on their in-service performance. For safety critical parts, such as aero-structural components, an understanding of how machining induced surface integrity characteristics influence fatigue behaviour is paramount to ensure reliable predictions regarding a component's service life. Although the primary objective of finish machining processes is to generate surfaces with desirable geometrical and topographical properties, mechanical, thermal, and chemical interactions which occur between the tool and workpiece also alter the characteristics of material in the subsurface layer [1]. Such alterations can have both desirable and unfavourable effects on component performance [2]. The term 'surface integrity' encompasses both the metallurgical and mechanical condition of surface and subsurface material [3]. Regarding the metallurgical state of titanium alloys, machining processes have been shown to affect the microstructure of a workpiece through induced subsurface strain leading to severe plastic deformation (SPD), typically characterised by distortion of the workpiece's crystallographic texture as it approaches the machined surface [4]. Phase changes and dynamic recrystallisation are other metallurgical alterations which have been reported to occur during the machining of titanium alloys and can result in the formation of features such as ultra-fine grained material, referred to as 'white layer' near the surface of a workpiece [5–7]. Mechanical alteration of subsurface material following machining can include changes to the near-surface residual stress state [8], as well as an increase in micro-hardness levels [9]. Under fatigue loading conditions, these alterations to the microstructure and mechanical properties of the subsurface can influence component fatigue life by effecting both crack nucleation and crack propagation behaviour in the altered subsurface region [10].

Despite the availability of literature which assesses the influence of cutting parameters on various aspects of surface integrity, few studies have evaluated the effects of machining on fatigue behaviour directly. While many manufacturers specify limits for surface integrity features such as the size of surface defects and SPD layer thickness, there remains a lack of understanding on their full implications on fatigue. Early models attempted to predict fatigue life based on surface topography features such as surface roughness metrics [11,12], however

* Corresponding author at: Department of Materials Science and Engineering, University of Sheffield, Sir Robert Hadfield Building, Mappin Street, Sheffield, S1 3JD, UK.
E-mail address: tchilderhouse1@sheffield.ac.uk (T. Childerhouse).

https://doi.org/10.1016/j.ijfatigue.2022.107054
Received 10 March 2022; Received in revised form 24 May 2022; Accepted 31 May 2022
Available online 8 June 2022

these have proven to be mostly inaccurate, particularly at the low roughness conditions attainable by modern finish machining processes. Under these circumstances, features occurring in the subsurface, such as residual stresses and subsurface microstructural condition, have been shown to be a more accurate indicator of performance [13,14].

It has been suggested that machining is primarily influential on fatigue performance in the high cycle fatigue (HCF) region due to the effects on a components crack initiation resistance [13], however a number of studies have identified that machining induced features also have significance in the low cycle fatigue (LCF) regime. Cox et al. [15] demonstrated that higher material removal rates (MRRs) during ball-nose milling of Ti–5Al–5V–5Mo–3Cr resulted in an increase in the layer thickness of the SPD microstructure. This was shown to have an unfavourable effect on LCF performance which was attributed to increased damage accumulation through activation of dislocation slip planes when machining with more aggressive cutting parameters. This was shown to result in strain localisation under fatigue loading, leading to the early onset of fatigue crack initiation. Interestingly, at higher MRRs, an increase in near surface compressive residual stresses was also observed, however the limited number of conditions explored in the study meant that the isolated influence of residual stress evolution was not assessed. Suárez Fernández et al. [16] showed that machining enhanced the LCF performance of Ti–6Al–2Sn–4Zr–6Mo forgings. The authors attributed this to near-surface compressive residual stresses which were postulated to be a more dominant mechanism to improve crack initiation resistance, compared to the effects of subsurface SPD and surface defects which could contribute to stress concentration at potential crack initiators. It was highlighted that the effects of underlying forging texture remained influential on fatigue performance following machining, due to its effect on crack propagation behaviour through the bulk of the material, which was unaffected by the machining process. While these studies show promising developments in improving the understanding of the role of machining on the fatigue behaviour of titanium alloys, further research is still required to fully understand how the combined effect of coexisting machining induced surface/subsurface anomalies influence material performance.

The presence of residual stress influences a material's ability to resist the initiation of a crack as well as its subsequent growth [17]. When a material is subjected to external loading, the stress intensity field acting at a potential crack initiating defect or at the crack tip itself can be determined by superposition of the applied and residual stresses [18]. When residual stresses act in a direction to resist crack opening, they can have a beneficial effect on fatigue performance. Compressive residual stresses for example, have been demonstrated to extend fatigue life by inhibiting crack initiation and growth following processes, such as machining [10] as well as shot peening [19]. Fig. 1 illustrates possible scenarios in which machining induced compressive residual stresses can influence fatigue failure. The influence of residual stress on crack initiation life is demonstrated in Fig. 1a. Surface defects typically left behind following machining, such as feed marks, can promote early crack initiation. Under sufficiently compressive residual stresses, shielding from the full range of stress intensity applied at the crack tip ΔK_{app}, as well as a reduction in the peak stress intensity K_{Max}, will increase the minimum defect size threshold a_{th}, such that additional fatigue damage accumulation would be required to nucleate a crack, thereby delaying crack initiation [18]. Fig. 1a also considers the distribution of machining induced residual stresses which typically display steep gradients as they approach their peak compressive level at a given depth beneath the surface. Under such conditions, it is possible that cracks propagating from the surface may arrest if the effective stress intensity range, ΔK_{eff} falls below that of the threshold range, ΔK_{th} due to increasing crack closure stresses [20]. In these circumstances, less energy may be required to nucleate a new crack, rather than continue to propagate the existing one. Fig. 1b demonstrates a reduction in the Stage II crack growth rate, da/dN due to residual stress induced

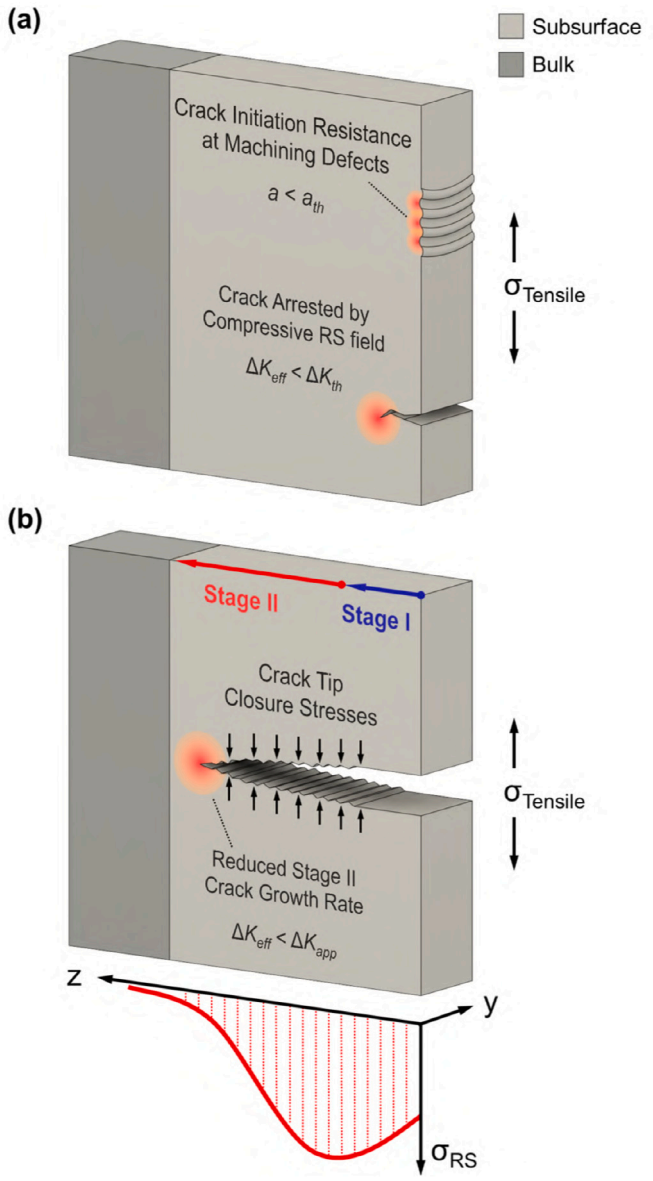

Fig. 1. Schematic illustrating the possible effects of machining induced compressive residual stresses on: (a) fatigue crack initiation and (b) crack propagation behaviour.

crack closure, reducing the effective stress intensity range at the crack tip below that of the applied range, i.e. $\Delta K_{eff} < \Delta K_{app}$ [18].

This study aims to evaluate the influence of cutting tool material, cutting parameter selection, and tool wear condition on the response of a combination of surface integrity related features including; (i) surface topography, (ii) microstructural alteration, and (iii) residual stress evolution when machining Ti–6Al–4V. The significance of these machining influenced features on fatigue behaviour was assessed using a four-point bend flexural test method. In addition to the use of more conventional coated cemented carbide (WC-Co) tooling, fatigue specimens have been machined using polycrystalline diamond (PCD) cutting tools. The superior high temperature performance offered by PCD tooling means that optimum machining performance is achievable at significantly higher cutting speeds and lower feed rates whilst continuing to maintain competitive MRRs [21]. Under such conditions, the thermomechanical interactions between the tool and workpiece will differ considerably compared to those experienced during coated carbide milling and as a result have the potential to significantly affect the surface integrity and fatigue performance of the component.

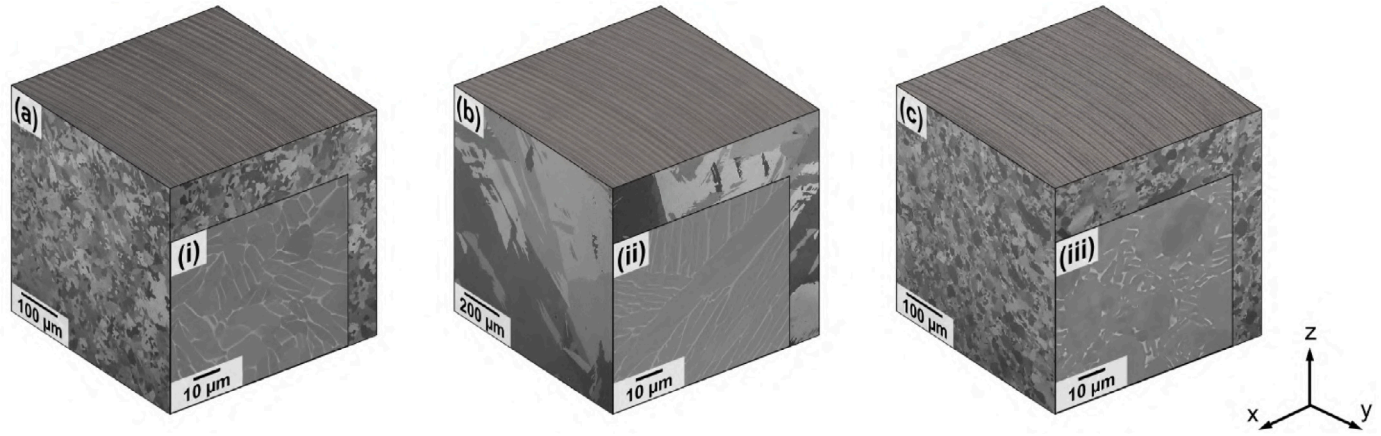

Fig. 2. Microstructures of the Ti–6Al–4V specimen parent material processed via the following routes: (a) FAST in the sub-β_t temperature region, (b) FAST in the super-β_t temperature region, and (c) uni-directionally (UD) rolled plate. High resolution BSE images of the respective conditions are shown in (i)–(iii).

Three different workpiece materials displaying unique microstructural properties have been selected to produce test specimens. These materials include wrought product in the form of unidirectionally rolled (UD) plate as well as material consolidated by field assisted sintering technology (FAST), a solid-state powder consolidation process [22]. Due to the recent emergence of more economical titanium alloy process routes such as FAST, there is a growing need to investigate the machining induced surface integrity and fatigue performance of these materials. Processing of the FAST material has been carried out by sintering in the sub and super β-transus (β_t) temperature regions for Ti–6Al–4V ($\beta_t \approx 995$ °C) to produce test coupons possessing fine and coarse grain structures. This has made it possible to assess the influence of machining on the fatigue behaviour of materials with different underlying microstructures.

2. Experimental method

2.1. Material processing routes

The microstructures of the Ti–6Al–4V material processed by the different routes explored in this study are shown in Fig. 2. The sub-β_t processed FAST microstructure consists of equiaxed primary alpha, α_p (~5 µm dia.) with lath-type secondary alpha, α_s dispersed between α_p clusters. In contrast, the super-β_t processed material shows a fully transformed β microstructure, comprised of large prior-β grains (~400 µm) containing lamellar α colonies. The UD rolled material displays a duplex microstructure of globular α_p (~12 µm) and lamellar α_s fractions.

The FAST Ti–6Al–4V specimens analysed in this research were taken from discs consolidated using a FCT Systeme GmbH Type H-HP D 250 spark plasma sintering system at Kennametal Manufacturing (UK) Ltd. The discs were of respective dimensions of 250 and 30 mm in diameter and thickness. Test coupons of dimensions 4.10 × 19 × 120 mm were extracted from each disc by wire-EDM prior to finish machining. Sintering processes have been demonstrated to be effective at producing fully dense titanium alloy components over a range of sub-melting point temperatures, extending to temperatures in the sub-β_t region for $\alpha+\beta$ alloys [23]. This capability means that materials with a variety of microstructural properties can be processed directly, without the requirement for post-sintering heat treatments. Fatigue test coupons were taken from two different FAST discs, consolidated at temperatures in the sub-β_t and super-β_t temperature regions for Ti–6Al–4V. The same methodology was employed for the production of each disc, which was as follows: The graphite ring mould was filled with powder, then placed within the upper and lower graphite hydraulic rams in the machine's vacuum chamber. The mould assembly was then pre-loaded to 5 kN to ensure electrical contact. Once the vacuum chamber was evacuated, the sintering cycle then followed a process of heating to the dwell temperature at a rate of 25 °C/min. Dwell temperatures of 970 and 1200 °C in the respective sub-β_t and super-β_t temperature regions were employed for the processing of each disc. Discs were then held at peak temperature conditions for a 60 min duration prior to cooling to ambient conditions at a rate of 6–8 °C/min. During processing, temperature measurements were taken with a pyrometer positioned at the interface between the powder and upper graphite ram. The applied ram pressure during processing of both discs was 35 MPa.

The FAST discs were produced using surplus additive manufacturing (AM) Ti–6Al–4V powder with a size distribution of 105–408 µm and therefore above the maximum particle size requirements for powder bed AM [25]. The powder morphology, shown in Fig. 3, displays

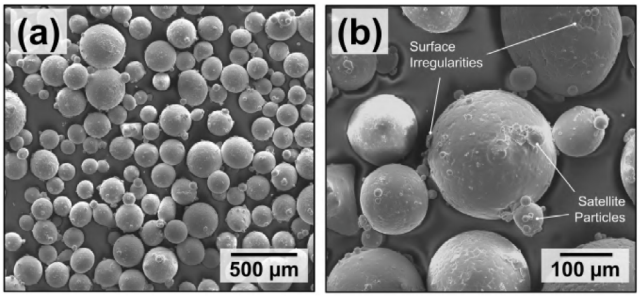

Fig. 3. SEM micrographs showing the morphology of the Ti–6Al–4V powder feedstock material used for the consolidation of the FAST billets: (a) Lower magnification image showing the presence of spherical and non-spherical particles and (b) a higher magnification image highlighting surface irregularities and satellite particles.

Table 1
Chemical composition of the initial Ti–6Al–4V powder and UD rolled material used in this work. All measurements given in wt.%.

Element	Al	V	C	Fe	O	H	N	Ti
UD rolled	5.88	4.10	0.01	0.25	0.21	<0.001	0.03	Bal.
FAST	6.12	3.94	0.03	0.16	0.10	<0.01	0.01	Bal.

Table 2
Static mechanical properties of the FAST Ti–6Al–4V material. Data obtained from uniaxial tensile testing of ASTM E8/E8M-16 [24] specimens extracted from the same FAST Ti–6Al–4V disc material.

Processing conditions	E [GPa]	UTS [MPa]	σ_y [MPa]	Elongation [%]
Super-β_t	108	835	757	8.3
Sub-β_t	118	901	833	11.1

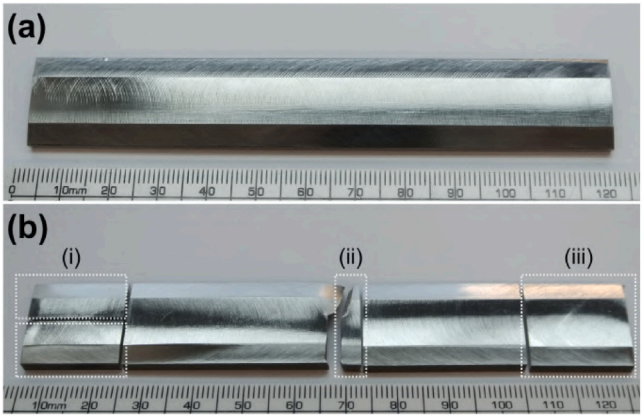

Fig. 4. Photographs of four point bend fatigue test specimens: (a) following machining showing typical feed mark striations, and (b) post fatigue failure. In (b) the specimen has been sectioned following failure to carry out analysis of (i) the machining effected microstructure, (ii) the fracture surface and, (iii) machining induced residual stresses.

surface irregularities, fused satellite particles, as well as the presence of non-spherical particles. Such defects can contribute to porosity related defects in AM processes [26], however previous studies have shown FAST to be significantly less sensitive to the quality of feedstock material [23,27]. The chemical composition of the powder feedstock material and static mechanical properties of the FAST material are provided respectively in Tables 1 and 2.

For the purposes of comparison with conventionally processed material, test coupons were also taken from UD rolled Ti–6Al–4V plate stock supplied by Rolls-Royce. Coupons were taken in orientations both parallel (UD-II) and perpendicular (UD-T) to the rolling direction.

2.2. Finish machining

Specimens were machined to their final geometry, shown in Fig. 4, using a DMG Mori DMU Evo 40 machining centre. A schematic illustrating the machining setup is shown in Fig. 5. In this configuration, a single face milling pass was carried out to generate each specimen's critical test surface, which would be subjected to the maximum applied tensile stress during fatigue loading. Respective cut dimensions for radial, a_e and axial, a_p cutter engagement were 19.0 and 0.50 mm. A radial offset between the cutter and specimen centres was applied at a distance of 2 mm to facilitate a thick-to-thin chip morphology. Following this operation, the adjacent chamfer surfaces were then machined in the same setup using the 5-axis capabilities of the machine tool. Surfaces were machined using a tooling setup provided by Seco Tools which consisted of a 25 mm diameter indexable square shoulder milling cutter (*R217.69-2525.3-10-4A*) installed in a HSK-A63 side lock holder. For all machining operations, Blaser Swisslube Vasco 7000 coolant was directed at the cutting edge via through tool delivery at a pressure of 50 Bar and a concentration of 5%–8%.

To compare the effects of various machining induced surface integrity features on fatigue behaviour, specimen test surfaces were generated employing six unique machining conditions. These were achieved by using three different grades of cutting inserts, used with both a new and pre-worn cutting edge. To attain this controlled pre-worn tool condition, inserts were subject to preliminary trials whereby a material volume of 100 cm^3 was machined from surplus Ti–6Al–4V UD rolled material. The machining operation and cutting parameters employed were identical to those used for face milling the test specimens. The tooling selected for this study comprised of two WC-Co insert grades, featuring different coating technologies, and a single uncoated PCD grade. A summary of the inserts selected with respective cutting parameters for cutting speed (V_c) and feed rate (f_z) is provided in Table 3. Parameters employed reflect those typical for industrial finishing processes with WC-Co tooling [28], whereas parameters selected for PCD machining are in the high speed/low feed range which has been demonstrated to offer extended tool life in similar applications by reducing forces on the cutting edge [29,30]. During the machining of each specimen test surface, cutting force data in the feed (F_f), cutting (F_{fN}), and axial (F_p) directions were captured through Kistler dynamometry hardware, which is shown in Fig. 5.

Table 3
Cutting tool grades and associated parameters selected for face milling of fatigue specimen test surfaces.

Tool Grade	Coating Composition	Speed, V_c [m/min]	Feed, f_z [mm/tooth]
F40M (WC-Co)	PVD[a] TiAlN-TiN	60	0.08
MS2500 (WC-Co)	CVD[b] TiCN-Al_2O_3	60	0.08
PCD05	Un-coated	200	0.03

[a]Physical vapour deposition;
[b]Chemical vapour deposition applied coating.

2.3. Four point bend fatigue test method

Fatigue testing was carried out using a four-point bend flexural loading configuration to generate a stress condition in each specimen as shown by the finite-element stress contour map in Fig. 6. In this arrangement, the maximum tensile stress applied to each specimen, S_{Max}, is located over a large region of the machined surface. Under these conditions, differences in the machining induced surface integrity will have a profound influence on fatigue behaviour. A similar test method has been used previously to study the influence of: (i) machining induced damage on the fatigue behaviour of Ti-5553 [15], (ii) the influence of crystallographic texture from upstream forging on the fatigue behaviour of Ti-6246 [16], and (iii) porosity distribution on the fatigue behaviour of AM Ti–6Al–4V [31]. In these studies, the technique has displayed a high level of sensitivity to machining conditions.

All tests were conducted under ambient conditions using a custom designed test device which distributed dynamic loading to each specimen through a pair of lower rollers, with the specimen supported by a pair of upper static rollers at a span distance, $L = 80$ mm. Loading was applied from a Nene 12 kN servo-hydraulic test machine controlled via a Moog Smartest One controller receiving load cell feedback. Each test was carried out employing sinusoidal loading conditions at a frequency of 5 Hz and a stress ratio of $R = 0.1$. For the UD rolled and sub-β_t processed FAST material, a maximum stress of $S_{Max} = 950$ MPa was applied, which was sufficient to induce local plasticity within the FAST sub-β_t material, with $S_{Max} = 1.14\sigma_y$. Owing to the lower strength of the FAST super-β_t material, testing was carried out at $S_{Max} = 850$ MPa, or equivalent to $1.12\sigma_y$. The total number of specimens tested for each machined condition was three for the FAST sub-β_t and FAST super-β_t material and four for the UD rolled material, with two orientated parallel (UD-II) and two perpendicular (UD-T) to the rolling direction.

2.4. Characterisation techniques

Low resolution microstructural analysis was carried out using cross-polarised light microscopy performed with a Nikon Eclipse LV150 optical microscope. For higher resolution imaging, required to characterise machining induced subsurface deformation, scanning electron microscopy (SEM) was performed with an FEI Inspect F50 field emission gun scanning electron microscope using secondary electron (SE) and backscattered electron (BSE) imaging. As characterisation of the machining induced microstructure was performed following fatigue failure, specimens were sectioned to remove material located outside the region of the material subjected to fatigue loading (as shown by Fig. 4b). This region of material was assumed to be representative of

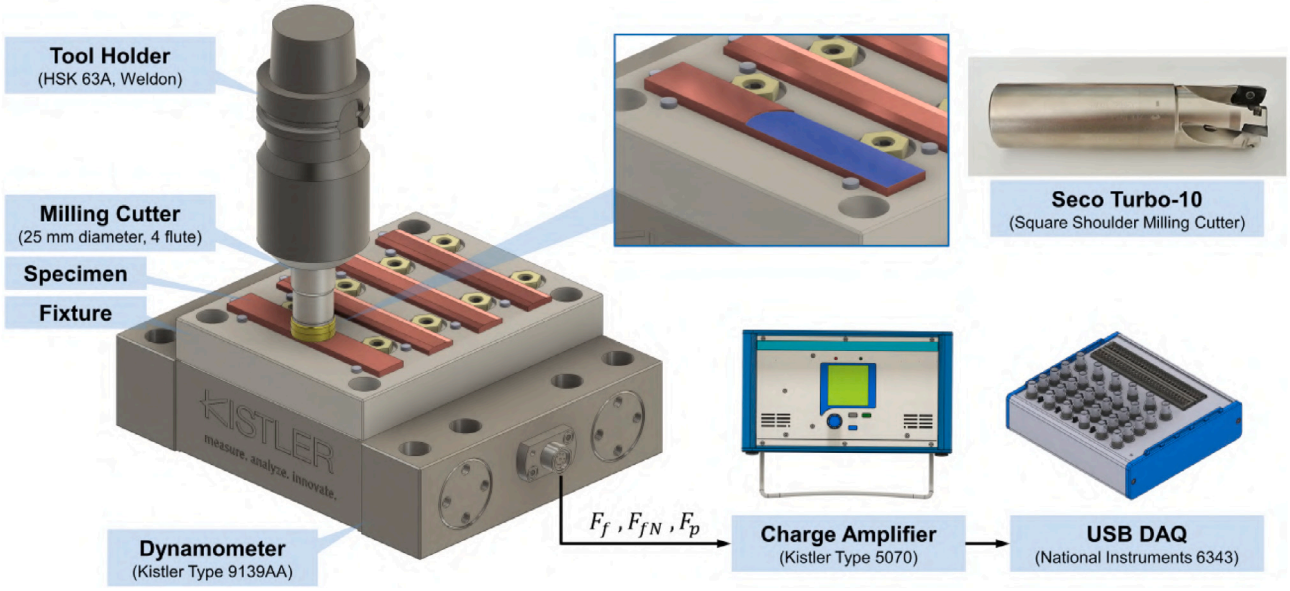

Fig. 5. Schematic illustrating the tool, workholding, and cutting force acquisition setup used to generate the fatigue specimen test surfaces.

the machined subsurface condition along the entire specimen length. The same SEM system was also used to carry out post-mortem fracture surface analysis to identify crack growth behaviour and microstructural features leading to failure. Prior to fatigue failure, the 3D surface topography of the machined surfaces were characterised using an Alicona InfiniteFocusSL optical 3D measurement system to obtain area-based 3D surface roughness metrics. Higher resolution imaging of the machined surfaces was carried out using a Hitachi TM3030 SEM system to identify the presence of machining induced surface anomalies and defects.

The near-surface residual stress distribution for each of the machined conditions was measured using an incremental hole-drilling method based on electronic speckle pattern interferometry (ESPI). Residual stress components in the feed, σ_x^{RS} and tangential, σ_y^{RS} directions were acquired with the measurement location positioned on the feed centre line of the specimen. Measurements were taken following fatigue failure, therefore to ensure that the residual stress state remained unaffected by fatigue loading stresses, measurements were taken from a non-stressed portion of the specimen, located outside the roller pairs (refer to Fig. 4). This location is assumed to be representative of the machining induced residual stress state along the entire length of the specimen. Measurements were conducted using a Stresstech Prism® system whereby the sample surface is illuminated with a coherent laser to construct a speckle pattern by diffuse light scattering, characteristic of the surface topography as well as any changes due to surface shifts. Holes were drilled using a 1.25 mm dia. drill at increments of 10 μm up to a depth of 50 μm, increments of 25 μm up to a depth of 150 μm, and at increments of 50 μm up to the final depth of 1 mm. The sample surface was imaged before and after each drilling increment to calculate the phase angle shift for each pixel, which was translated to determine surface displacement. The near-surface residual stress depth profiles were then calculated from the optically measured surface displacement data applying a Young's modulus of 118 GPa for the UD rolled and FAST sub-β_t material conditions and 108 GPa for the FAST super-β_t condition. A Poisson's ratio of 0.342 was applied for all material conditions.

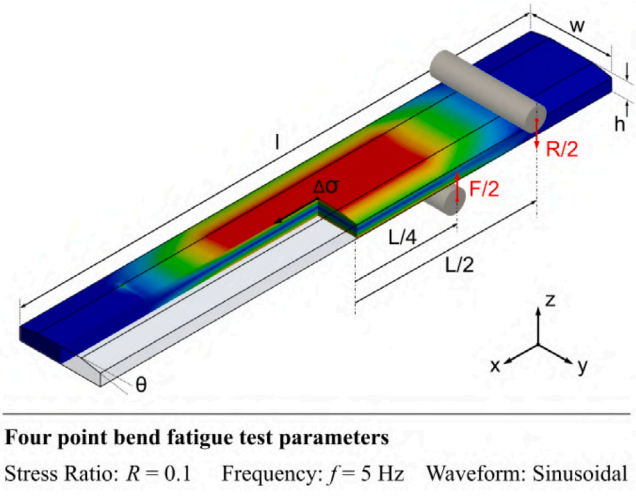

Fig. 6. Schematic representation of the four point bend fatigue test method and specimen geometry with superimposed FEA stress distribution. Respective dimensions for specimen length l, width w, and height h, are 120, 19, and 3.60 mm with a chamfer angle θ, of 10°.

3. Results and discussion

3.1. Cutting tool condition prior to specimen machining

The cutting edge condition of the pre-worn tooling is shown in Fig. 7 and tool wear and cutting edge radii metrics are provided in Table 4. The tooling used featured a range of edge radii, r_0 in their as-received condition, with the PCD tooling featuring the sharpest cutting edge. The MS2500 grade featured the largest edge radii, which can be attributed to a thicker coating layer in comparison to that applied to the F40M grade. In the pre-worn condition, the WC-Co grades experienced wear predominantly to the nose of the tool, at the location where the tool engages with the un-cut chip. Wear scars on the WC-Co tooling show the presence of abrasive scarring, WC grain pullout, and the loss of the coating layer. Levels of tool wear experienced by the MS2500 grade were higher than that of the F40M grade, however in both cases wear levels were below that of the flank wear limit criteria, VB = 200 μm typically used by manufacturers and therefore could be considered representative of tooling close to the end-of-life condition. In contrast, the PCD05 tooling experienced considerably higher levels of wear characterised by severe mechanical fracture which resulted in

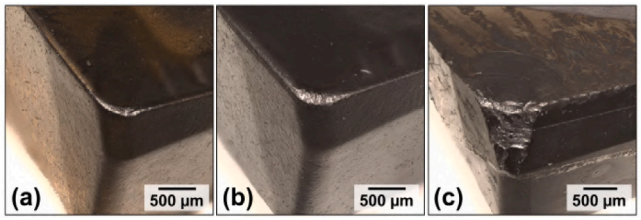

Fig. 7. Tool condition following the removal of 100 cm^3 of material during preliminary wear trials: (a) Shows the condition of the F40M WC-Co grade, (b) the MS2500 WC-Co grade, and (c) the PCD05 grade.

Table 4
Tool wear and cutting edge radii metrics for tooling in the as-recieved and pre-worn conditions.

Tool grade	$r_0[\mu m]$	$r_1[\mu m]$	VB_{Max} $[\mu m]$
F40M (WC-Co)	27	67	133
MS2500 (WC-Co)	46	93	196
PCD05	7.7	n/a	967

wear beyond that of typical wear limit criteria. The pre-worn edge radii metrics, r_1 provided in Table 4 give an indication on the effect of wear on the change in cutting edge geometry. For the WC-Co tooling, loss of tool material at the cutting edge contributed to an increase in the cutting edge radii as well as a rougher edge profile. In contrast the pre-worn PCD tooling featured a chamfer-type geometry, with a chamfer width ~300 μm.

3.2. Fatigue performance

The fatigue cycles to failure for all of the conditions included in the investigation are given in Fig. 8. For all cases failure has occurred in the HCF range (N_f > 20k cycles). A comparison between the material conditions shows the longest fatigue lives were achieved by the UD rolled (II) material (i.e. when σ_{Max} was orientated parallel to the rolling direction). Anisotropic fatigue performance of UD rolled titanium alloys is typical due to the strong *c*-axis (basal-transverse) texture developed during the plane strain rolling process [32]. Loading perpendicular to the *c*-axis has shown longer fatigue life than when loading parallel to the *c*-axis, which is in agreement with results from the present study. This is attributed to the greater number of available slip systems when loading perpendicular to the *c*-axis, and therefore, greater plastic strain accumulation can occur during cyclic straining, which relaxes the applied stresses. Comparable fatigue lives were displayed by the FAST sub-β_t and UD rolled (T) material, whereas the shortest fatigue lives were achieved by the FAST super-β_t processed material, despite being subjected to a lower stress magnitude.

A comparison between the various machining conditions reveals that fatigue lives were shortest following machining with the unworn PCD tooling, with PCD machined specimens achieving on an average 60% fewer cycles to failure compared to their WC-Co machined counterparts. Comparable performance was typically achieved by specimens machined with the F40M and MS2500 WC-Co unworn tooling for the two UD rolled and the FAST super-β_t material conditions, however a 50% improvement in fatigue life was observed for the FAST sub-β_t condition following machining with the MS2500 grade. For specimens machined with WC-Co tooling in the pre-worn condition, tool wear was shown to contribute to a reduction in average fatigue life by 15%. In contrast, wear to the PCD tooling resulted in extended fatigue lives by an average of 40% compared to specimens machined with unworn tools. Although the increase in fatigue life resulting from wear to the PCD tooling was displayed across the entire test program, the drop in fatigue life following wear to the WC-Co tooling was only displayed by the FAST and UD rolled (II) material conditions.

An error range of 0.33–16.91% and a mean error of 8.23% of total fatigue life was calculated across the entire test programme based on the measured standard deviation taken from two repeat tests carried out for each of the FAST material conditions and a single repeat for each of the UD rolled conditions. This level of error was typically below that of the observed differences in fatigue life.

To investigate the influence of machining condition on crack initiation and growth life independently, interrupted testing was carried out with the UD rolled (II) material following machining with the MS2500 and PCD05 tooling in the as-received condition. Tests were stopped at 90% of the average cycles to failure for the given condition and the specimen surfaces were each inspected for the presence of surface cracks under high resolution SEM. This analysis revealed that no surface cracks had formed at this stage in the overall fatigue life of the component. This suggests that fatigue life is dominated by the crack initiation period, or if in the case that subsurface cracks had formed, which were undetectable during inspection, by both the initiation and very early crack growth stages.

3.3. Fractography

Fatigue failure of all specimens occurred with crack formation in the maximum stress region of the specimen highlighted in Fig. 6. Specimen fracture surface features are presented for the UD rolled and FAST material conditions in Figs. 9 and 10 respectively. In the UD rolled (II) material, crack initiation can be seen to have occurred from a faceted α_p grain which has been subject to transgranular cleavage along the basal plane (labelled 'A' in Fig. 9a-i). This failure mechanism is typically displayed by α+β titanium alloys due to dislocation pile up at grain boundaries arising from unfavourably, or "hard", orientated α grains. This results in grain faceting due to localised shear stress concentration [33]. The initiating facet is located ~5 μm beneath the machined surface and is surrounded by α_p grains displaying evidence of cleavage and slip band formation (highlighted by the dotted lines in Fig. 9a-i). A similar crack initiation mechanism can be observed for the FAST sub-β_t material, whereby crack initiation has also occurred from a faceted α_p grain located in the near surface region of the material (labelled 'A' in Fig. 10a-i). Conversely, the UD rolled (T) material does not show typical crack initiation from a faceted grain, but instead shows multiple cracks which have formed at an anomalous surface defect (labelled 'D' in Fig. 9b-i). This defect is believed to be adhered workpiece material, or machining "pick-up" from the built up edge material on the tool, deposited on the machined surface which has led to crack initiation due to local stress concentration. (The influence of machining induced surface defects on fatigue behaviour is discussed further in Section 3.6). It is notable that initiation at surface defects, such as that shown in Fig. 9b-i, was only observed in one instance shown following machining with the F40M tooling in the as-received condition. Crack initiation from faceted α_p grains located in the subsurface was observed in all other cases for the UD rolled and FAST sub-β_t specimens, irrespective of machining condition. Furthermore, the inspection of a second F40M machined specimen revealed subsurface faceting of α_p being the cause of crack initiation.

In the FAST super-β_t material, crack initiation can be seen to have occurred from a faceted prior-β grain located at the machined surface (labelled 'B' in Fig. 10b-i). This grain has been subject to transgranular cleavage along α colony grain boundaries. This mechanism of crack initiation was observed on all of the inspected FAST super-β_t fracture surfaces irrespective of machining condition.

Away from the crack initiation point, in the bulk and subsurface regions of the material, the fracture surfaces of the UD rolled material display fatigue striations (Figs. 9a-ii and b-ii) on faceted surfaces, with the direction of striations aligned at varying angles from one grain to another. It is well established that the formation of striations occurs with their orientation perpendicular to the direction of crack growth [20,34], this indicates that the local crack growth direction is

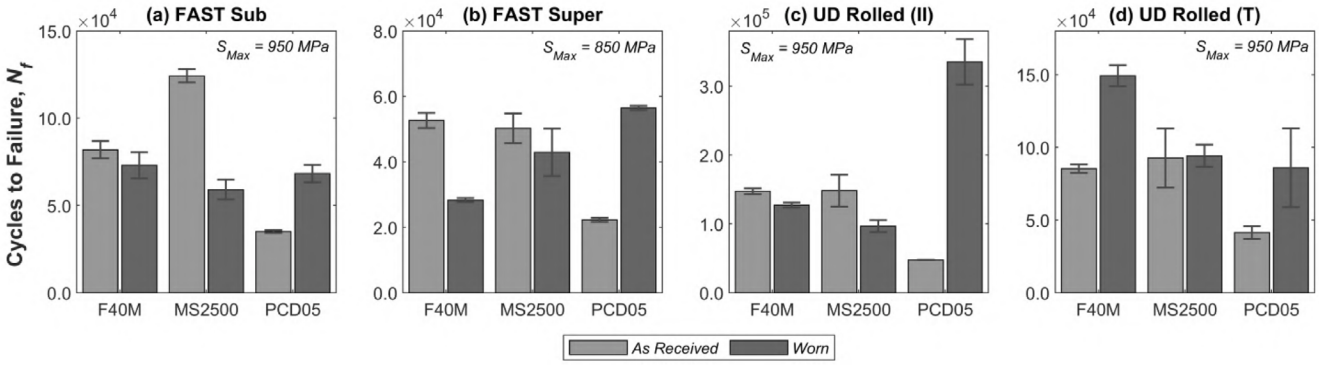

Fig. 8. Comparison of the different machining conditions on fatigue life for: (a) the FAST sub-β_t, (b) the FAST super-β_t, (c) the UD rolled (σ_{Max} parallel to rolling direction) and, (d) the UD rolled (σ_{Max} perpendicular to rolling direction) material condition. Error bars denote ± one standard deviation.

dependent on individual grain orientation. In non-striated areas, the surface shows evidence of monotonic tensile failure. Similar fracture features have been reported in previous studies investigating the fatigue behaviour of UD rolled Ti–6Al–4V [32] and has been attributed to the restriction of the major crack growth direction by unfavourably orientated grains, causing the crack to be diverted around a less resistant path. This causes static tensile failure of the remaining ligaments resulting in the monotonic fracture features observed. The FAST sub-β_t fracture surface also displays cleavage facets with striated/monotonic regions (Fig. 10a-ii) which are on a similar scale to those present on the UD rolled material indicative of a combination of local fatigue crack growth and monotonic tensile failure. As the crack length approaches the lower edge of the specimen, a distinct transition from striated faceted regions to a fully dimpled surface was observed for all material conditions. This transition can be seen to be located approximately 600–800 μm from the lower edge of the fracture surface. These fine equiaxed dimpled regions (Figs. 9a-iv, 9b-iv, and 10a-iii) show evidence of microvoid formation and coalescence typical of a ductile failure, which has occurred as the crack has propagated to a length sufficient for unstable growth. In this final or "fast" fracture region, the material has consumed very few fatigue loading cycles. Similar ductile fracture regions were also observed in the material beneath the chamfer surfaces of the specimen.

In comparison to the other material conditions tested, the coarse grained FAST super-β_t material displays a considerably rougher fracture surface. This results from the coarser faceted regions (Fig. 10b-ii) present at the fracture surface, which are on a scale comparable to that of the prior-β grains. Micrographs illustrating the crack path as it propagates through the microstructure of the FAST sub-β_t and super-β_t are shown respectively in Figs. 10a-iv and 10b-iv. The crack through the FAST sub-β_t material displays a straight path whereas the crack through the FAST super-β_t material displays a noticeably more convoluted path. This is a result of crack propagation along lamellar α grain boundaries at the α–β interface and the redirection of the crack along prior-β grain boundaries as it encounters α colonies possessing a crystallographic texture less favourably orientated for crack growth. This has produced the dimpled ('C') and striated ('D') regions seen on the fracture surface (Fig. 10b-iii). Convoluted crack paths have been shown to offer higher levels of crack propagation resistance in titanium alloys possessing colony type 'macrozones', whereas these same microstructures can also display low crack initiation resistance properties due to their poor suppression of slip band formation when compared to fine grained material [35]. This is explanatory of the poor fatigue life of the FAST super-β_t material in comparison to the other conditions, as interrupted testing carried out to 90% N_f, indicated that for the fine grained UD rolled material, the total fatigue life is dominated by crack initiation under the loading conditions employed. Further evidence of poor crack initiation resistance of the FAST super-β_t material was also indicated by presence of additional secondary cracks which formed in the highly stressed region of the specimen on planes parallel to the fatal crack. Secondary crack formation was not observed for the other material conditions.

Fatigue striations located at a distance of approximately 300–500 μm from the crack initiation point comparing each material condition are shown in Fig. 11. At this crack length, a striation spacing distance in the order of ~0.83 μm/cycle can be observed for the UD rolled (II) material, ~0.56 μm/cycle for the FAST sub-β_t material, and ~1.6 μm/cycle for the FAST super-β_t material. The striation spacing was found to vary significantly as a function of crack length, indicating an increase in crack growth rate as the crack propagated further from the initiation point. Due to this variation, it is difficult to compare the crack propagation rate for different machining conditions, as locating a striated facet for a precise crack length was not possible. However, based on the spacing of the striations presented in Fig. 11, an estimation can be made regarding the crack propagation life of the specimen, based on an assumed total crack length of 3 mm. (This assumes that no fatigue cycles were consumed in the final ~600 μm fast fracture region). This would estimate a crack propagation life below 5% N_f for the UD rolled material and below ~10% N_f for the FAST sub-β_t and super-β_t material conditions. These estimations are expected to be over-predictions as they are based on striations located close to the initiation point, where the crack growth rate was at is slowest. Despite this, they are in agreement with the results from the interrupted fatigue testing which indicated no crack formation at 90% N_f for the UD rolled (II) material.

3.4. Analysis of machining induced residual stresses

The subsurface residual stress profiles following machining are shown in Figs. 12 and 13 for the UD rolled and FAST material conditions respectively. Although each profile was measured to a total depth of 1 mm, the distributions given provide the residual stress state up to 250 μm, as beyond this depth, stresses had converged to their bulk value (±50 MPa). For all conditions, similar profiles and stress magnitudes can be seen to have been induced when measurements were taken in either the feed, σ_x^{RS} or normal, σ_y^{RS} directions. Specimens machined with WC-Co tooling display a predominantly compressive residual stress distribution, whereby surface stresses which are typically compressive, increase to their maximum compressive level at a depth of ~25–75 μm and then fall to the bulk stress level at a depth of ~100–200 μm. In contrast, following machining with the unworn PCD tooling, profiles typically show negligible differences when comparing near-surface stresses to those in the bulk (Figs. 12b and 13a), and in some instances (Fig. 12a), a tensile stress component can be seen in the first 50 μm of the specimen. In the pre-worn condition however, stresses induced by the PCD tooling show compressive profiles, resembling those following WC-Co machining.

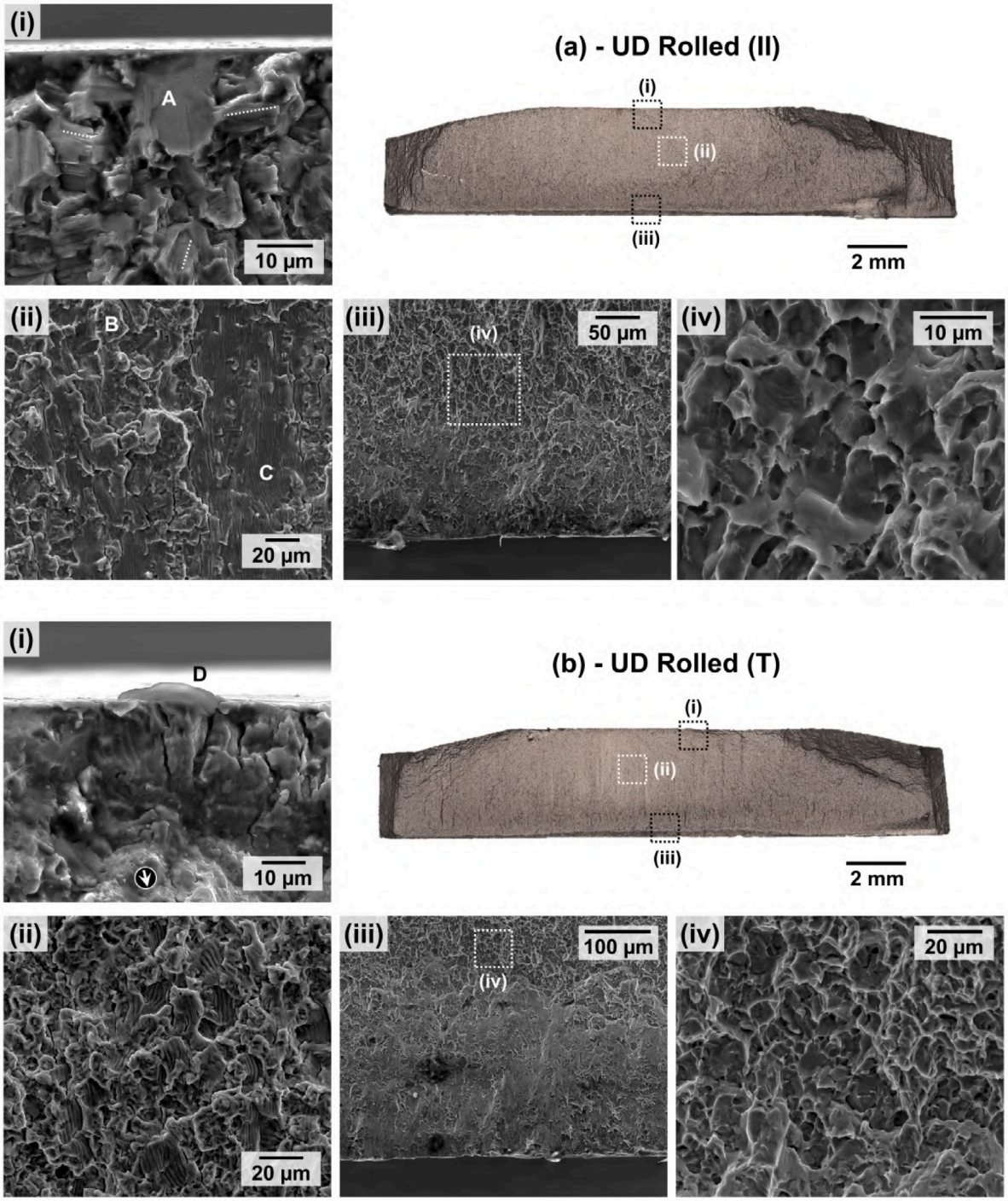

Fig. 9. SE images of fracture surface features. (a) The UD rolled (II) material showing: (i) crack initiation from a faceted α_p grain (labelled 'A'), (ii) fatigue striations (labelled 'C') and monotonic regions (labelled 'B') away from the point of crack initiation, (iii) the surface approaching the lower edge of the specimen showing the transition to ductile fracture, and (iv) dimples present in the fast fracture region. (b) The UD rolled (T) material showing: (i) the initiation of multiple surface cracks originating from surface "pick-up" (labelled 'D'), (ii) fatigue striations and monotonic regions in the bulk material, (iii) the transition to ductile fracture, and (iv) dimples present in the fast fracture region. The arrows shown indicate the local crack growth direction.

To highlight the influence of cutting conditions resulting from the different tooling and cutting parameters on residual stress, metrics have been taken from each profile for features including: (i) the area beneath the residual stress distribution, (ii) the near-surface residual stress, $\sigma_{x,\ surf}$ (taken at a depth of 20 µm), (iii) the peak compressive stress, $\sigma_{x,\ peak}$, and (iv) its corresponding subsurface location, z_{peak}. These metrics have been plotted in Fig. 14. As stresses in the feed and normal directions display similar tendencies, the metrics plotted in Fig. 14 correspond with those in the feed direction as this corresponds with the direction of applied stress under fatigue loading. It is notable, however, that under test conditions, stresses will not be perfectly orientated in this direction and normal stresses will also partially contribute to the materials behaviour. Fig. 14a highlights a trend between compressive stress in the near-surface with those throughout the profile. Specimens machined with the PCD tooling imparted the lowest levels of stress, whereas the MS2500 grade, which featured the larger edge radii of the

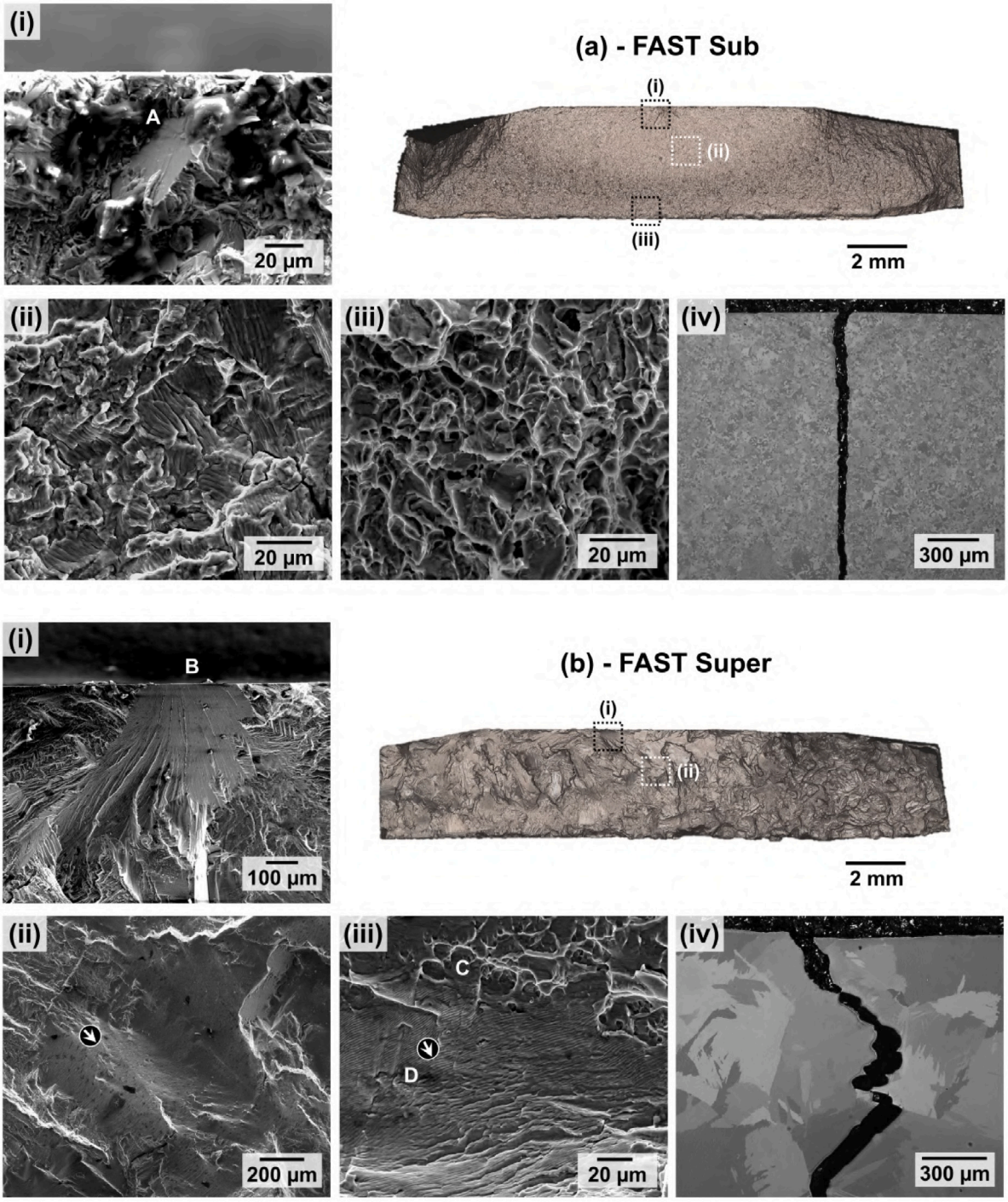

Fig. 10. SE images of fracture surface features. (a) The FAST sub-β_t material showing: (i) crack initiation from a faceted α_p grain (labelled 'A'), (ii) fatigue striations and secondary cracking, (iii) dimples located towards the lower edge of the specimen indicating ductile fracture, (iv) the crack in section showing a straight crack path. (b) The FAST super-β_t material showing: (i) crack initiation located at a faceted prior-β grain (labelled 'B'), (ii) coarse faceted surfaces, (iii) dimpled regions (labelled 'C') and fatigue striations on the facet surfaces (labelled 'D'), and (iv) the crack in section showing a convoluted crack path. The arrows shown indicate the local crack growth direction.

two WC-Co tools, induced significantly higher levels of compressive stress than the F40M grade. Shen et al. [36] also demonstrated an increase in the compressive residual stress component as a result of an increase in tool edge radii. This was attributed to an increase in the thickness of the ploughed material layer passing through the deformation zone. This resulted in deeper penetration of plastic and elastic tensile strain into the subsurface, which following material springback are retained as compressive residual stresses. Fig. 14b shows the correlation between maximum compressive residual stress and its corresponding subsurface depth. A trend can be observed showing that in material where a higher level of compressive stress is present its corresponding depth beneath the surface increases. This trend indicates that as the ploughing effect increases, both the thickness of the ploughed material layer and the level of imparted tensile strain increase.

Comparing the residual stress distribution for new vs. pre-worn tooling shows an increase in compressive stress following wear to the

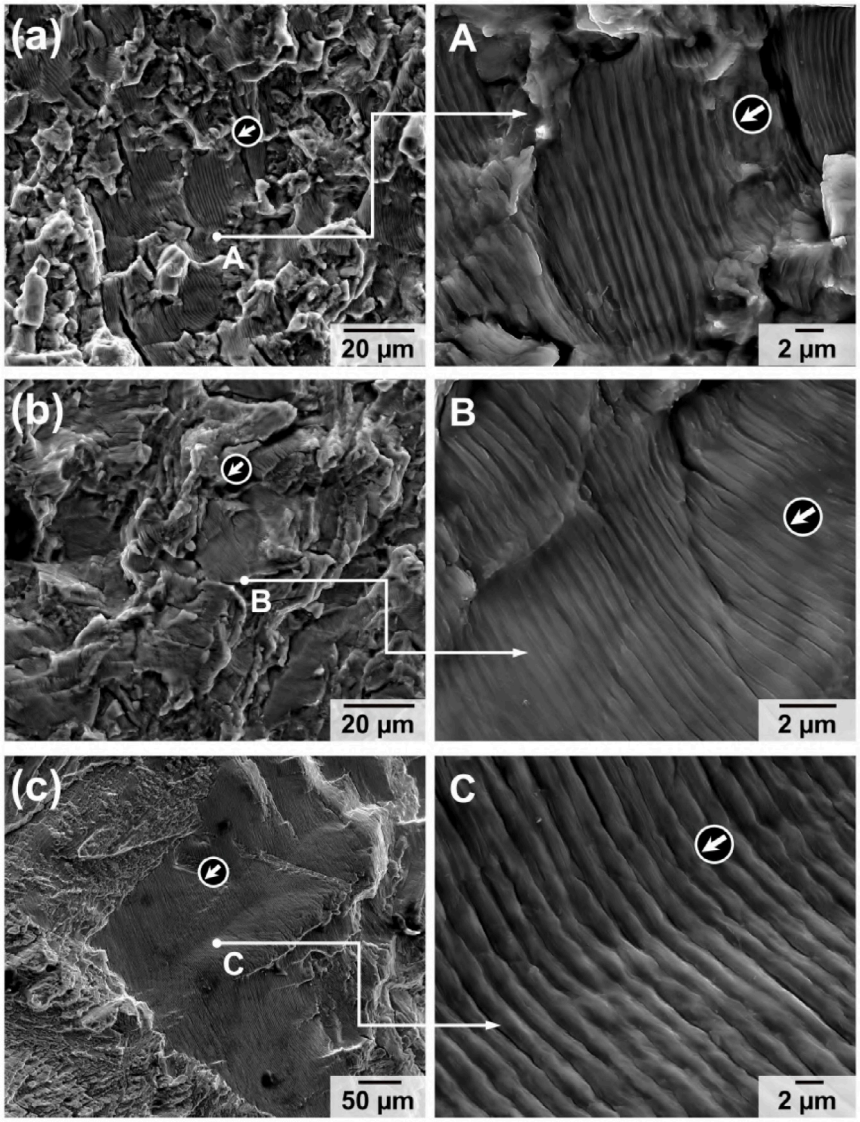

Fig. 11. High magnification SE images showing fatigue striations present on faceted surfaces at crack lengths of ~300–500 µm from the crack initiation point. (a) Shows striations on the UD rolled (II) material suggesting a crack growth rate of ~0.83 µm/cycle, (b) shows striations on the FAST sub-β_t material suggesting a crack growth rate of ~0.56 µm/cycle, and (c) shows striations on the FAST super-β_t material suggesting a crack growth rate of ~1.6 µm/cycle. The arrows indicate the direction of crack growth and the loading direction is normal to the image plane. Fracture surfaces correspond to specimens machined with unworn F0M grade tooling.

PCD tooling. This can be attributed to the change in cutting edge microgeometry following tool wear, as the worn chamfer-type geometry would contribute to higher levels of workpiece ploughing, in a similar manner to the mechanism discussed previously. Changes in the edge geometry of WC-Co tooling following tool wear resulted in an increase in cutting edge radii. Despite this, residual stresses following machining with the pre-worn WC-Co tooling saw similar as-received/pre-worn levels for the F40M grade, whereas more compressive stresses were observed following wear to the MS2500 grade. To explain this finding, the influence of the mechanical interaction occurring between the tool and workpiece cannot be considered in isolation and thermal interactions must also be addressed. The local loss of the tool's coating layer and an increase in cutting edge roughness are expected to have contributed to higher levels of friction between the tool and workpiece, generating higher cutting temperatures. Under such conditions, the workpiece will experience more extreme thermal gradients in the subsurface, inducing a tensile residual stress component. The higher levels of wear experienced by the MS2500 tooling, when in comparison to the F40M, may have contributed to a more significant thermally induced stress component, which has resulted in a greater offset to the mechanically induced compressive stresses following tool wear. As thermal gradients do not penetrate deep into the material, their effect is more significant close to the surface. This is evident when comparing the as-received/pre-worn WC-Co tooling which typically display less compressive residual stresses as they approach the surface (Figs. 12 and 13). Thermally induced tensile residual stresses are also expected to have been induced following machining with unworn PCD tooling. This is due to the high surface speeds and low feed rates employed which generate higher temperatures due to increased heat concentration on the workpiece surface and less heat evacuation through the chip. These conditions are expected to have contributed to the near-surface tensile residual stress components displayed by the PCD machined material.

The correlation between the area beneath the compressive residual stress distribution and normalised fatigue life is shown in Fig. 15a. Fatigue data has been normalised based on material condition to account for differences in underlying fatigue performance displayed by the different materials tested. For each condition, the normalised fatigue performance has been calculated with respect to the specimen achieving the longest fatigue life following machining with an unworn cutting edge. For material machined with unworn tooling, a strong trend is

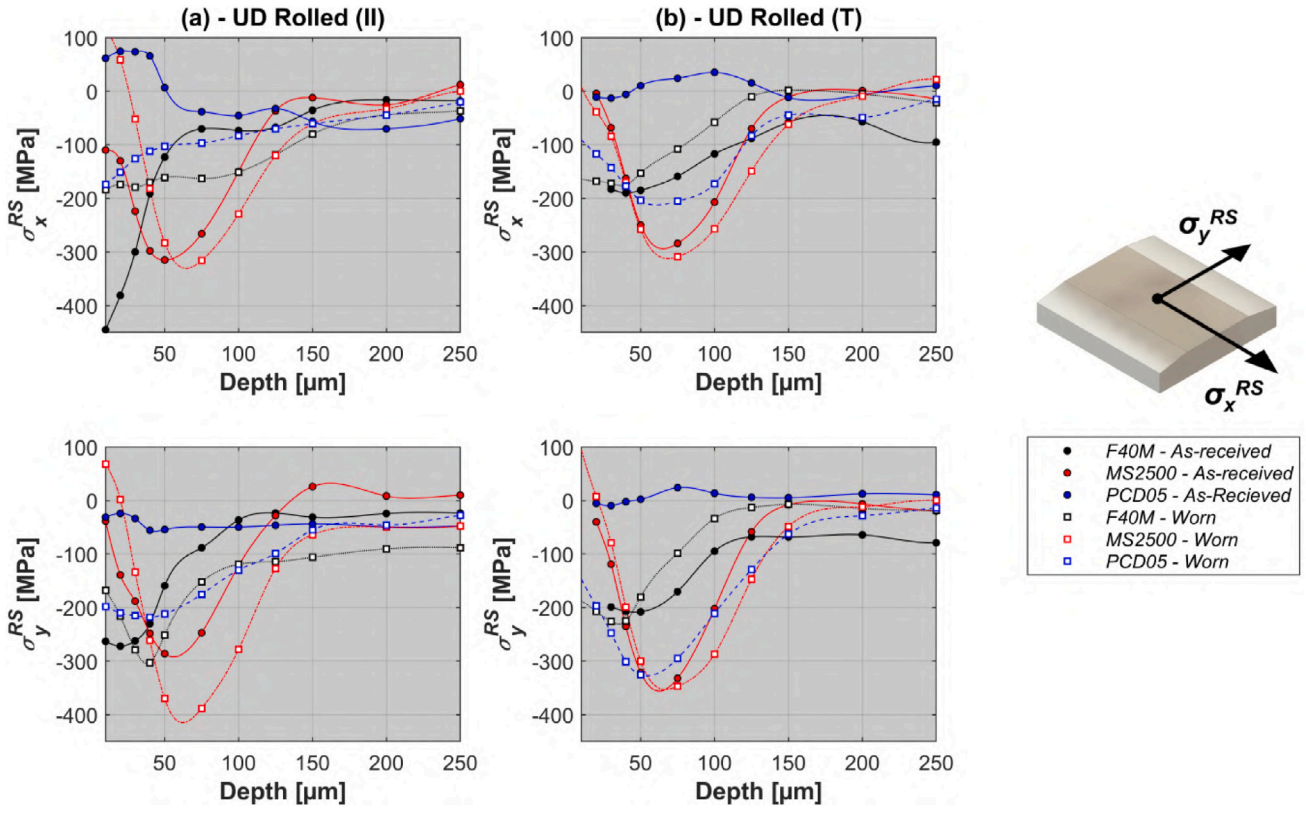

Fig. 12. Profiles showing the distribution of subsurface residual stress in the feed, σ_x^{RS} and normal directions, σ_y^{RS} for: (a) The UD rolled material where σ_{Max} is applied parallel to the rolling direction and (b) where σ_{Max} is applied perpendicular to the rolling direction.

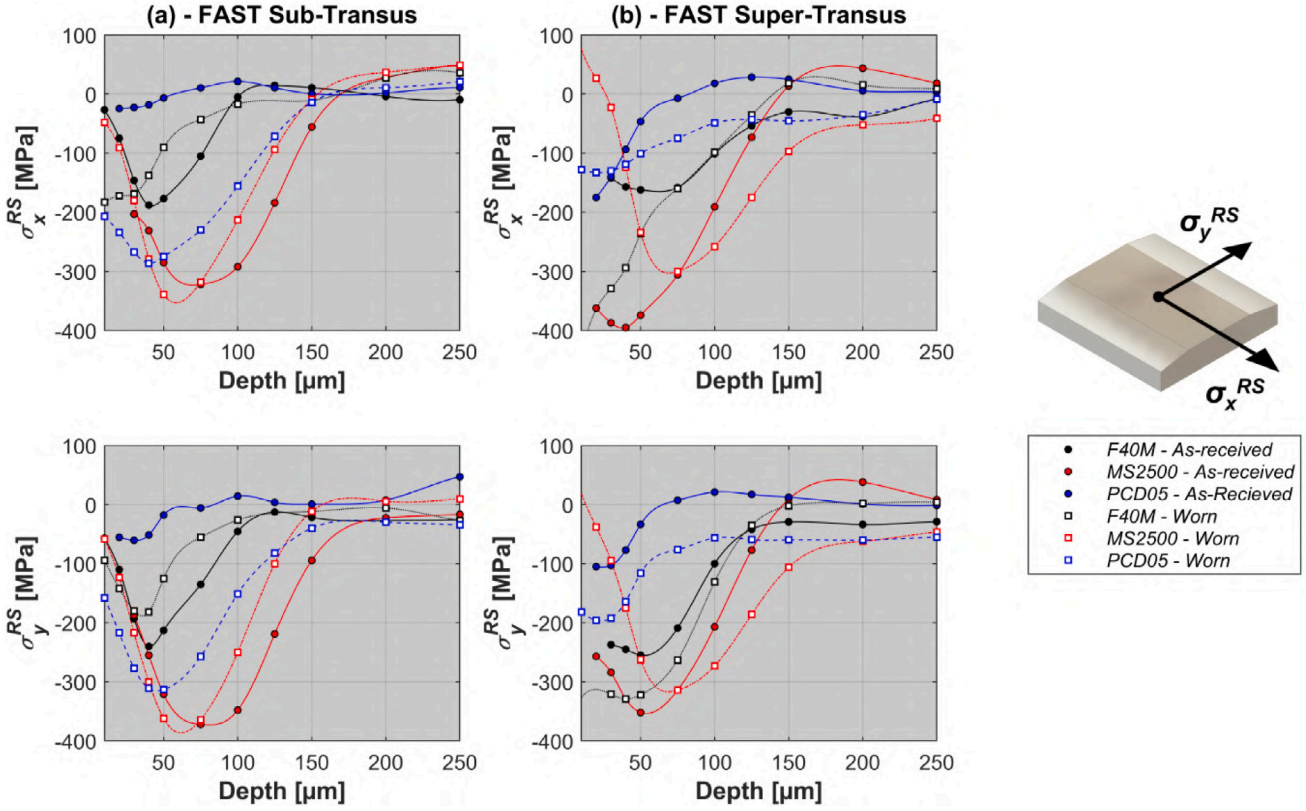

Fig. 13. Profiles showing the distribution of subsurface residual stress in the feed, σ_x^{RS} and normal directions, σ_y^{RS} for: (a) The FAST sub-β_t material and (b) the FAST super-β_t material.

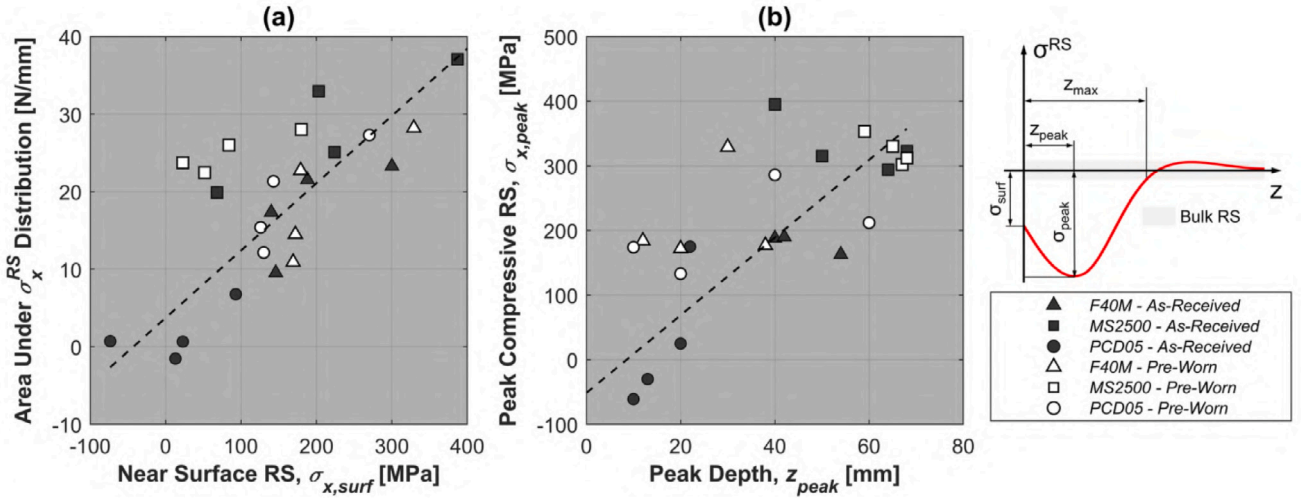

Fig. 14. (a) The correlation between the area beneath the compressive residual stress distribution, σ_x^{RS} and near-surface compressive residual stress, $\sigma_{x,\ surf}$ taken at a depth of 20 μm. (b) The correlation between peak compressive residual stress, $\sigma_{x,\ peak}$ and its depth location, z_{peak}.

observable, highlighting an increase in fatigue life, as induced residual stresses become more compressive. For material possessing a fine grain structure, such as the UD rolled and FAST sub-β_t specimens, which displayed fatigue lives dominated by crack initiation, this improvement in fatigue life can be attributed to predominately an increase in crack initiation resistance. This mechanism of residual stress influenced crack initiation suppression is depicted in Fig. 1a: local stress intensity sites at machining induced surface defects, or unfavourably orientated grains in the subsurface, are shielded from the full stress intensity range, ΔK and are subjected to a lower level of peak stress intensity K_{Max}. Whether a reduction in either ΔK or K_{Max} has a more significant effect on initiation life cannot be determined from the present study, as at low R values such as 0.1, both shielding from ΔK and a reduction in K_{Max} are achieved concurrently. Further investigation testing at an R value in the 0.8–0.9 range would reduce K_{Max} without influencing ΔK and could provide evidence whether a reduction in K_{Max} alone offers a fatigue life enhancement.

For the coarse grained FAST super-β_t, where crack propagation is expected to have had a more significant influence of overall fatigue life, the influence of residual stress on Stage II crack propagation through the residual stress field will have played a more significant role on fatigue performance. This mechanism is depicted by Fig. 1b, whereby the rate of crack growth, da/dN during Stage II linear propagation is proportional to ΔK, as governed by the Paris–Erdogan equation [20]:

$$\frac{da}{dN} = C(\Delta K)^m \tag{1}$$

Where C and m are material coefficients dependent on environmental conditions, stress ratio, and microstructure. For a material subject to no residual stress, the stress intensity range, ΔK is equivalent to the difference between the maximum and minimum stress intensity factors under the applied load cycle. Under conditions where residual stresses are present, the relative magnitudes of the applied and residual stress can result in a reduction in the stress intensity range subjected to the crack tip such that $\Delta K^{eff} < \Delta K^{app}$. This scenario is demonstrated by *Case C* in Fig. 16, where the residual stresses present are sufficient for shielding of the applied load at the crack tip due to the closure of the crack over a portion of the loading cycle. The stress intensity range, ΔK^{eff} for a material where residual stresses are present is given by [18]:

$$\Delta K^{eff} = K_{Max}^{eff} - K_{Min}^{eff} \tag{2}$$

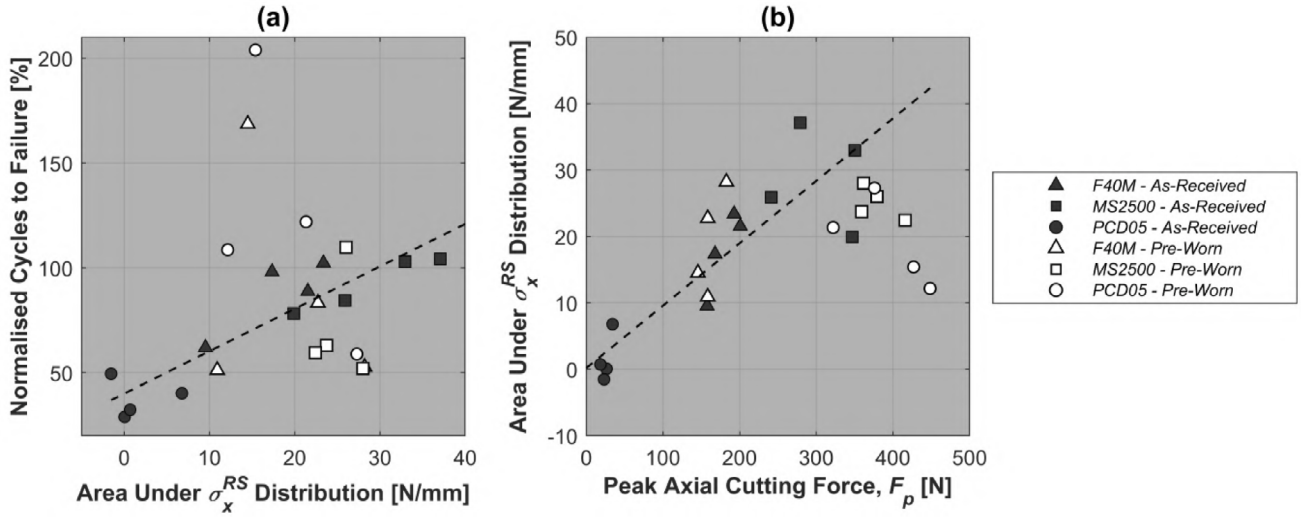

Fig. 15. (a) The correlation between the area beneath the compressive residual stress distribution, σ_x^{RS} and fatigue cycles to failure normalised based on material condition. (b) The influence of peak axial cutting force, F_p on the area beneath the compressive residual stress distribution, σ_x^{RS}.

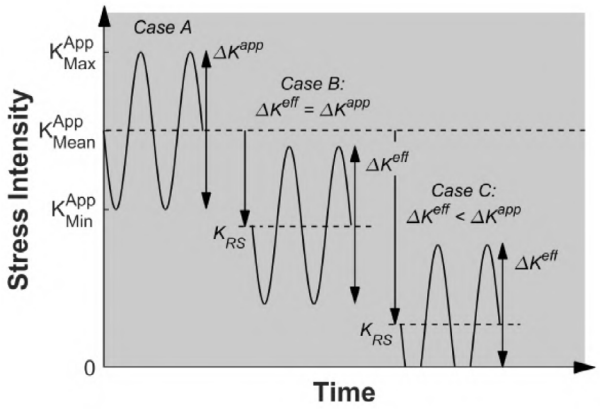

Fig. 16. Schematic showing the influence of residual stress on the stress intensity at a crack tip, K_{Max}. *Case B* shows how the presence of compressive residual stresses can reduce K_{Max}. *Case C* demonstrates partial shielding from the applied load at the crack tip due to the presence of sufficiently high residual stress such that, $\Delta K^{eff} < \Delta K^{app}$ in the stress free scenario, *Case A*.
Source: Image adapted with permission from [18].

where:

$$K^{eff} = \begin{cases} K^{app} + K^{RS}, & \text{if } K^{app} + K^{RS} \geq 0 \\ 0, & \text{if } K^{app} + K^{RS} < 0 \end{cases} \quad (3)$$

where K^{RS} is the stress intensity contribution from the residual stress. At the applied stress ratio, $R = 0.1$, stress levels are low enough such that the compressive residual stresses present are sufficient for $K^{eff}_{Min} = 0$ for a portion of the loading cycle. In this scenario, the stress intensity range can be determined by substituting Eq. (3) into Eq. (2):

$$\Delta K^{eff} = K^{app}_{Max} + K^{RS} \quad (4)$$

Substituting this expression into Eq. (1) yields:

$$\frac{da}{dN} = C\left(K^{app}_{Max} + K^{RS}\right)^m \quad (5)$$

Eq. (5) demonstrates how the presence of compressive residual stresses, such as those induced by the machining processes in this study, can reduce the Stage II crack growth rate and extend the fatigue life of a component. To compare the effects of the various machining induced residual stress state on the crack growth rate, K^{RS} must be evaluated for the different machining conditions. For a through thickness edge crack of length a, the stress intensity contribution from the residual stress is given by [18]:

$$K^{RS}(a) = \int_0^a \sigma^{RS}(x)\omega_p\{a, x\}\, dx \quad (6)$$

where the weight function, ω_p is the stress intensity arising from a unit force applied to the crack face at x which is dependent on the crack geometry and boundary conditions. From Eq. (6) it is evident that the increase in fatigue life, owing to a reduction in crack propagation rate due to the presence of K^{RS}, is proportional to the area beneath the compressive residual stress distribution.

Considering the crack initiation location for the UD rolled and FAST sub-β_t specimens, which was typically observed in α_p grains ~10–40 μm beneath the machined surface, the influence of surface residual stress level is expected to have a less significant influence on fatigue life than the stress distribution beneath the surface. For example, a stress distribution comprised of a lower compressive surface stress, but a peak stress penetrating deeper beneath the surface, may offer better fatigue life than a shallow distribution with a more compressive surface stress. This is due to the fact that crack nucleation and early stages of crack propagation would have to occur through a region of material subject to a higher average level of compressive residual stress. Similar findings have also been observed when investigating the effects of residual stresses induced following shot peening, where it was found that residual stress distribution was a better indicator of fatigue life than surface stress [19]. It is notable that in the present study, higher levels of compressive stress were coupled with a greater depth of penetration. This is due to the relationship between the ploughed layer thickness and residual stress distribution which has been previously discussed. Therefore, cutting parameters which were able achieve higher levels of compressive residual stress, also offered the advantage of an increased depth of penetration.

Fig. 15b correlates the peak axial cutting forces with the compressive residual stress distribution. A strong correlation is shown, highlighting higher levels of induced residual stress as cutting forces increase. This is due to the effect of cutting parameters and geometry which cause an increase in the ploughed material layer, correspond with an increase in the ploughing force component. Interestingly it can be observed that although the higher levels of wear to the MS2500 and PCD tooling resulted in an increase in F_p, this did not correspond with an increase in compressive residual stress. This is expected to be due to the effect of higher cutting temperatures contributing to a tensile stress component and thereby offsetting the compressive stresses.

3.5. Microstructural analysis of machining induced damage

Although a strong correlation was observed between compressive residual stress and fatigue life for material machined with a new cutting edge, results for material machined with worn tooling no longer display this relationship. This is suggestive that additional surface integrity features, introduced when machining with worn tooling, such as subsurface microstructural alterations, also influence fatigue life. Fig. 17 shows the subsurface microstructural condition of the UD rolled material following machining. The subsurface microstructural condition for the FAST sub-β_t and super-β_t materials are shown respectively in Figs. 18 and 19. Each micrograph has been annotated to show the depth of microstructural alteration of the SPD layer. Characterisation has been carried out in both the X–Z and Y–Z planes. Sweeping of grains in the direction of V_c, as is typically observed as a result of machining, was predominately seen in the Y–Z plane, whereas swept grains were less distinguishable in the X–Z plane. In this plane, the depth of microstructural alteration was distinguished more clearly by compression of the grain structure.

For all materials, similar observations were made with respect to the effect of machining condition on the thickness of the SPD layer. Following machining with an unworn cutting edge, material machined with WC-Co tooling resulted in higher levels of deformation than those machined with PCD, which resulted in a SPD layer thickness under 2.5 μm in the most severe case (Fig. 18c): otherwise the subsurface microstructure was non-distinguishable from the bulk material (Figs. 17c and 19c). Comparing the two WC-Co tool grades, reveals higher levels of microstructural deformation following machining with the MS2500, 10–13 μm, compared to the F40M grade, ~6 μm. This difference can be explained by the effects of cutting edge radius. The larger radii of the MS2500 tool will have increased the volume of material subjected to a negative rake angle, thereby leading to thicker layer of ploughed material which does not contribute to the chip volume flowing up the rake face of the tool. This imparts a greater amount of shear and compressive strain on the subsurface material, which, in addition to contributing to higher level of compressive residual stress, also contributes to an increase in the depth and level of SPD. A similar deformation response in Ti–6Al–4V, as a result of cutting edge geometry, has been reported by Brown et al. [7]. The lower levels of deformation observed following machining with the unworn PCD tooling can also be attributed to the effects of the considerably sharper cutting edge radii and lower feed rate employed during cutting, which are expected to have resulted in lower levels of ploughing induced microstructural deformation.

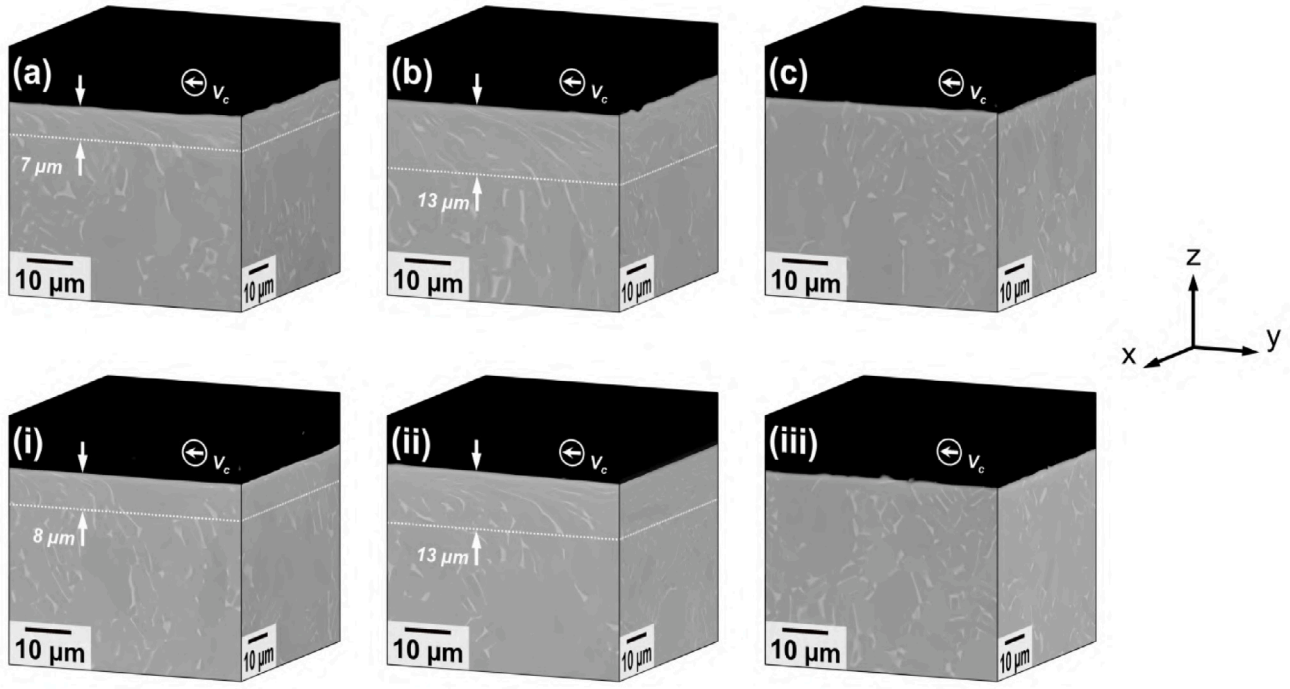

Fig. 17. BSE images of the subsurface microstructural condition of the UD rolled material following machining with: (a) the F40M, (b) the MS2500, and (c) the PCD05 tool grades in their as-received condition. Respective microstructural conditions following machining with tooling in the pre-worn condition are shown in (i)–(iii). Cutter feed is in the x-direction and rotation is clockwise about the z-axis.

Microstructural deformation as a result of machining has been linked previously to a reduction in fatigue crack initiation life of Ti-5553 [15] and has also been shown to have a negligible effect on fatigue following the machining of Ni-based superalloys, provided the deformed layer did not exceed a 10 μm limit [5]. In the present study, the detrimental effects associated with microstructural damage accumulation in the material prior to fatigue loading are shown to be less significant than the beneficial effects of compressive residual stress. This is demonstrated by the better fatigue performance of the WC-Co in comparison to the PCD machined material, despite higher levels of SPD. These finding highlight how microstructural damage as a result of machining can be tolerated, and can have a negligible detriment

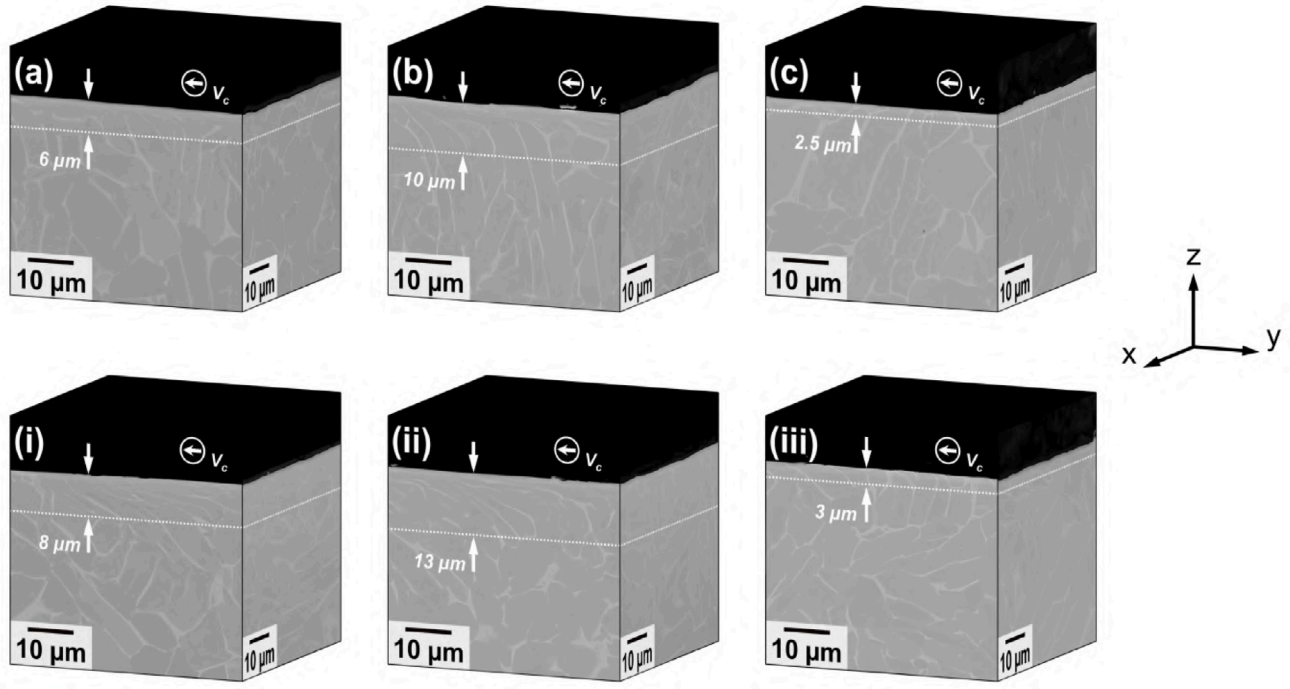

Fig. 18. BSE images of the FAST sub-β_t subsurface microstructural condition following machining with: (a) the F40M, (b) the MS2500, and (c) the PCD05 tool grades in their as-received condition. Respective microstructural conditions following machining with tooling in the pre-worn condition are shown in (i)–(iii). Cutter feed is in the x-direction and rotation is clockwise about the z-axis.

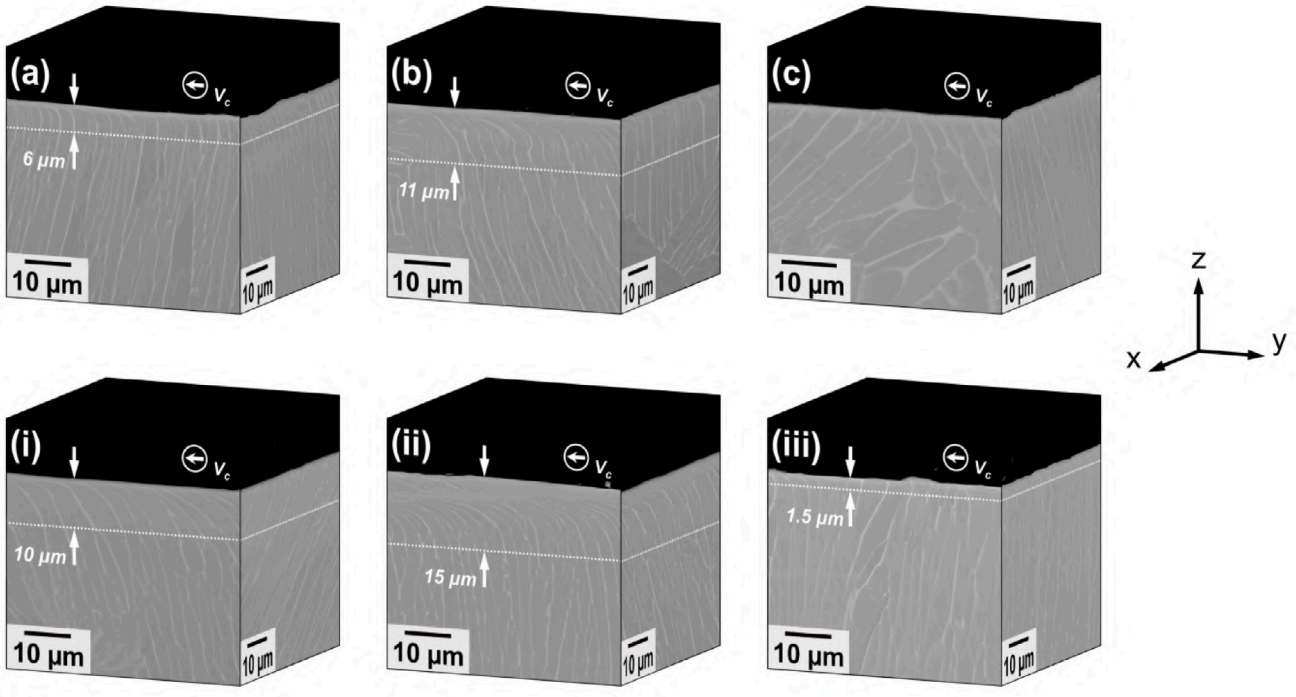

Fig. 19. BSE images of the FAST super-β_t subsurface microstructural condition following machining with: (a) the F40M, (b) the MS2500, and (c) the PCD05 tool grades in their as-received condition. Respective microstructural conditions following machining with tooling in the pre-worn condition are shown in (i)–(iii). Cutter feed is in the x-direction and rotation is clockwise about the z-axis.

on fatigue life, provided they are combined with fatigue enhancing compressive residual stresses.

In most instances, similar fatigue performance was achieved following machining with the F40M compared to the MS2500 grades, despite higher levels of compressive residual stress associated with the MS2500 grade. It is possible that the more severe microstructural deformation following MS2500 milling may account for the negligible improvement in fatigue life, as the enhancing effects of compressive residual stress are counteracted by machining induced damage accumulation which has contributed to a reduction in crack initiation resistance. Following machining with pre-worn tooling, the reduction in fatigue life observed when machining with WC-Co tools can also be attributed to this increase in SPD. Interestingly, despite the high levels of tool wear and high cutting forces associated with the worn PCD tooling, the levels of deformation observed were considerably less than those seen following WC-Co machining and the increase in the SPD layer thickness was negligible compared to material machined with new PCD tooling. Under these conditions, the significant increase in compressive residual stress has resulted in a fatigue life improvement, with little detrimental effect from microstructural deformation.

During WC-Co machining, the mechanism by which compressive residual stress and microstructural deformation are induced both coincide with ploughing imparted strain (elastic residual strain in the case of residual stress and plastic strain in the case of SPD). Therefore, cutting conditions which result in a higher level of ploughing will increase both compressive residual stresses and the severity of SPD. In comparison, during PCD machining the same ploughing mechanism has resulted in a much more significant effect on residual stress, whilst having a negligible effect on microstructure. It is possible that the increase in deformation rate during machining at the higher cutting speeds employed during machining with the PCD tooling have had a strain rate hardening effect. This has led to an increase in the materials resistance to plastic strain, which appears to be more dominant than any thermal softening which may also have occurred at the higher cutting speeds. Similar effects of cutting speed on microstructural deformation characteristics have also been reported by Li et al. [37]. Whilst the effects of higher strain rates will have increased the resistance to plastic strain of the material, strain rate is expected to have less significance regarding the material's elastic modulus. Therefore, the level of mechanically induced elastic residual strain will be largely unaffected by cutting speed. Hence, resulting in the increase in compressive residual stress following wear to the PCD tooling.

3.6. Assessment of machined surface condition and topography

The machined surface condition examined under BSE microscopy for the UD rolled material is shown in Fig. 20. Various machining induced surface anomalies can be identified including; (i) micro-welded material "pick-up" deposited from the tool, (ii) surface micro-cracks, and (iii) surface smearing. Similar inspection for materials process via FAST revealed that such features were typical regardless of material condition. A comparison between the different cutting tool grades indicates higher levels of "pick-up" and larger adhered particles when machining with the WC-Co tool grades. This can be attributed to higher cutting forces in comparison to those observed during PCD machining, which have contributed to high pressures exerted on built-up edge (BUE) adhered to the cutting edge (as shown in Fig. 21). The fracture surface analysis revealed that whilst the majority of cracks initiated at unfavourably orientated α_p grains in the subsurface, a single instance showed crack initiation occurring from the machined surface at a "pick-up" protrusion (annotated "D" in Fig. 9b-i) of a similar scale to those identified on the machined surface. Although similar "pick-up" protrusions have been shown to contribute to local stress intensification and can contribute to early crack nucleation [38], the findings in the present study indicate that the near-surface compressive residual stresses can suppress the fatigue limiting effects of these imperfections. This is evidenced by the subsurface crack initiation, which was identified on the majority of fracture surfaces, irrespective of the level of surface "pick-up". Furthermore, the longer fatigue lives of the WC-Co compared to the PCD machined specimens, the latter displaying considerably less severe "pick-up", suggests that a certain

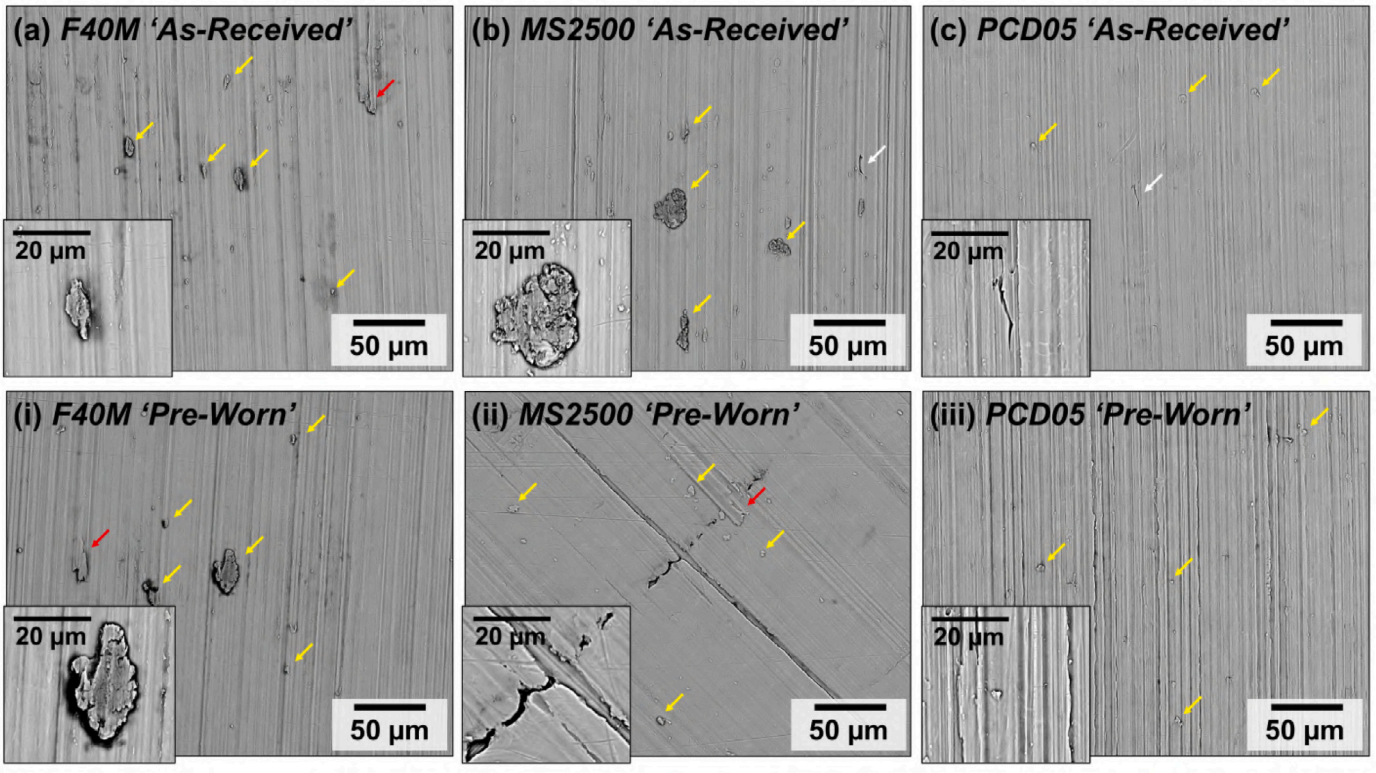

Fig. 20. BSE images of the UD rolled surface condition following machining with: (a) the F40M, (b) the MS2500, and (c) the PCD05 tool grades in their as-received condition. Respective surfaces following machining with tooling in the pre-worn condition are shown in (i)–(iii). Machining induced surface anomalies are highlighted showing micro-welded Ti–6Al–4V "pick up" deposited from the tool (yellow arrows), surface micro-cracking (white arrows), and material smearing (red arrows). Cutter feed direction is from left-to-right.

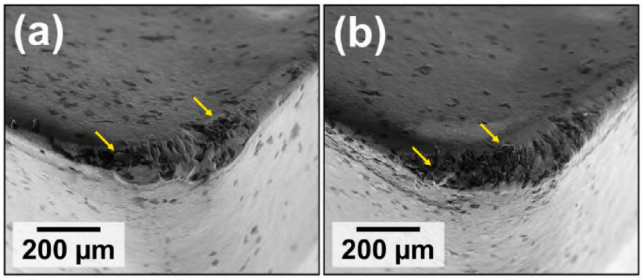

Fig. 21. SE images of: (a) the F40M and (b) the MS2500 worn cutting edges showing the presence of adhered material (yellow arrows) with a composition confirmed to be similar to the Ti–6Al–4V workpiece material by energy-dispersive X-ray spectroscopy (EDS) analysis.

level of machining induced surface imperfections can be acceptable due to the overriding influence of residual stress.

When machining with pre-worn cutting edges, the severity of surface defects was shown to increase. This was evident from larger scale "pick-up" particles on the machined surface in the case of machining with worn WC-Co tooling. Wear to both WC-Co and PCD tools contributed to more severe machining, or feed marks imparted on the machined surface. These can be seen by the deep groves following machining with the worn MS2500 tooling (Fig. 20ii) and the folded ridges following machining with the worn PCD tool (Fig. 20iii). It is expected that such defects would contribute to higher levels of stress concentration at the machined surface in comparison to the topological surface condition following machining with new cutting edges. However, as the majority of cases identified crack initiation to have occurred in the subsurface, it is expected that the surface defects such as those presented in Fig. 20 have less influence on fatigue crack initiation than the effects of the subsurface microstructural condition. Further work, whereby surface defects are removed either by polishing or etching processes, may offer benefit in discriminating between the effects of surface vs. subsurface machining induced anomalies.

Table 5
Surface roughness metrics for areal surface roughness, S_a and kurtosis (sharpness), S_{ku} taken from the machined surfaces of the UD rolled specimens. (Values of error denote ± one standard deviation).

Tool grade	Tool condition	S_a[µm]	S_{ku}[µm]
F40M	As-received	1.56 ± 0.04	3.82 ± 0.23
MS2500		1.31 ± 0.25	4.67 ± 0.86
PCD05		1.57 ± 0.14	3.60 ± 0.31
F40M	Pre-worn	1.40 ± 0.13	4.11 ± 0.17
MS2500		1.37 ± 0.19	4.70 ± 1.13
PCD05		1.62 ± 0.14	3.39 ± 0.10

It is notable that areal surface roughness metrics (provided in Table 5) indicate no statistically significant differences between the various machined conditions. This highlights that differences in the topological features associated with the machining methods employed in the study are below those which can be characterised with areal surface roughness metrics obtained using optical techniques.

4. Conclusions

This paper presents a comprehensive study on the influence of machining induced surface integrity characteristics on the high cycle fatigue performance of Ti–6Al–4V of different microstructural conditions using a four-point bend fatigue test configuration. Fatigue life has been shown to vary significantly with respect to cutting tool microgeometry, cutting parameter selection, and tool wear. The influence of residual stress distribution, subsurface microstructural condition, and the presence of machining induced surface defects/anomalies were assessed

regarding their effect on fatigue life, with a detailed study on their influence on the mechanisms of crack initiation and propagation.

Machining induced compressive residual stresses were found to be the primary factor for improving fatigue life due to their suppression of crack initiation and propagation. The deleterious effects of microstructural SPD and surface defects, such as "pick-up" of adhered workpiece material, were found to have a less significant effect on fatigue life. Such anomalies were demonstrated that they could be tolerated when combined with sufficient levels of compressive residual stress. Under these circumstances, crack initiation at surface defects was shown to be suppressed in the majority of cases, with cracks instead nucleating at unfavourably orientated α_p grains in the subsurface.

Compared to WC-Co milling at conventional cutting parameters, high speed PCD finishing resulted in a 60% reduction in component fatigue life, despite contributing to considerably lower levels of microstructural deformation and surface defects. This was attributed to lower levels of compressive residual stress following machining with the PCD tooling. Tool wear when machining with WC-Co tooling was shown to result in a reduction in fatigue life of ~15%. This was presumed to be due to a reduction in crack initiation resistance as a result of increased microstructural deformation and surface defects, which were caused by a higher volume of ploughed material when machining with worn tooling. In contrast, wear to PCD tooling resulted in a fatigue life improvement due to an increase in compressive residual stress.

Declaration of competing interest

The authors declare that they have no known competing financial interests or personal relationships that could have appeared to influence the work reported in this paper.

Acknowledgements

This study was funded by the EPSRC Industrial Doctorate Centre in Machining Science (EP/L016257/1) as well as Seco Tools and Element Six. The authors would like to acknowledge Rolls-Royce for the supply of the uni-directionally rolled Ti–6Al–4V material.

Appendix A. Supplementary data

Supplementary material related to this article can be found online at https://doi.org/10.1016/j.ijfatigue.2022.107054.

References

[1] Liao Z, Murray J, Speidel A, Ushmaev D, Clare A, Axinte D, et al. International journal of machine tools and manufacture surface integrity in metal machining - part I : Fundamentals of surface characteristics and formation mechanisms. Int J Mach Tools Manuf 2021;162(December 2020):103687. http://dx.doi.org/10.1016/j.ijmachtools.2020.103687.

[2] la Monaca A, Murray JW, Liao Z, Speidel A, Robles-Linares JA, Axinte DA, et al. Surface integrity in metal machining - part II: Functional performance. Int J Mach Tools Manuf 2021;164(March):103718. http://dx.doi.org/10.1016/j.ijmachtools.2021.103718.

[3] Ulutan D, Ozel T. Machining induced surface integrity in titanium and nickel alloys : A review. Int J Mach Tools Manuf 2011;51(3):250–80. http://dx.doi.org/10.1016/j.ijmachtools.2010.11.003.

[4] Xu X, Zhang J, Liu H, He Y, Zhao W. Grain refinement mechanism under high strain-rate deformation in machined surface during high speed machining Ti6Al4V. Mater Sci Eng A 2019;752(March):167–79. http://dx.doi.org/10.1016/j.msea.2019.03.011.

[5] Herbert C, Axinte DA, Hardy M, Withers P. Influence of surface anomalies following hole making operations on the fatigue performance for a nickel-based superalloy. Trans ASME, J Manuf Sci Eng 2014;136(5):1–9. http://dx.doi.org/10.1115/1.4027619.

[6] Brown M, Crawforth P, M'Saoubi R, Larsson T, Wynne B, Mantle A, et al. Quantitative characterization of machining-induced white layers in Ti–6Al–4V. Mater Sci Eng A 2019;764(July):138220. http://dx.doi.org/10.1016/j.msea.2019.138220.

[7] Brown M, M'Saoubi R, Crawforth P, Mantle A, McGourlay J, Ghadbeigi H. On deformation characterisation of machined surfaces and machining-induced white layers in a milled titanium alloy. J Mater Process Technol 2022;299(September 2021):117378. http://dx.doi.org/10.1016/j.jmatprotec.2021.117378.

[8] M'Saoubi R, Outeiro JC, Chandrasekaran H, Dillon OW, Jawahir IS. A review of surface integrity in machining and its impact on functional performance and life of machined products. Int J Sustain Manuf 2008;1(1–2):203–36. http://dx.doi.org/10.1504/IJSM.2008.019234.

[9] Jawahir IS, Brinksmeier E, M'Saoubi R, Aspinwall DK, Outeiro JC, Meyer D, et al. Surface integrity in material removal processes: Recent advances. CIRP Ann 2011;60(2):603–26. http://dx.doi.org/10.1016/j.cirp.2011.05.002.

[10] Choi Y. A study on the effects of machining-induced residual stress on rolling contact fatigue. Int J Fatigue 2009;31(10):1517–23. http://dx.doi.org/10.1016/j.ijfatigue.2009.05.001.

[11] Maiya PS, Busch DE. Effect of surface roughness on low-cycle fatigue behavior of type 304 stainless steel. Metall Trans A 1975;6(10):1761–6. http://dx.doi.org/10.1007/BF02642305.

[12] Taylor D, Clancy OM. The fatigue performance of machined surfaces. Fatigue Fract Eng Mater Struct 1991;14(2–3):329–36. http://dx.doi.org/10.1111/j.1460-2695.1991.tb00662.x.

[13] Novovic D, Dewes RC, Aspinwall DK, Voice W, Bowen P. The effect of machined topography and integrity on fatigue life. Int J Mach Tools Manuf 2004;44:125–34. http://dx.doi.org/10.1016/j.ijmachtools.2003.10.018.

[14] Sasahara H. The effect on fatigue life of residual stress and surface hardness resulting from different cutting conditions of 0 . 45 % C steel. Int J Mach Tools Manuf 2005;45:131–6. http://dx.doi.org/10.1016/j.ijmachtools.2004.08.002.

[15] Cox A, Herbert S, Villain-Chastre J-P, Turner S, Jackson M. The effect of machining and induced surface deformation on the fatigue performance of a high strength metastable β titanium alloy. Int J Fatigue 2019;124(February):26–33. http://dx.doi.org/10.1016/j.ijfatigue.2019.02.033.

[16] Suárez Fernández D, Wynne BP, Crawforth P, Fox K, Jackson M. The effect of forging texture and machining parameters on the fatigue performance of titanium alloy disc components. Int J Fatigue 2021;142:105949. http://dx.doi.org/10.1016/j.ijfatigue.2020.105949.

[17] Coules HE, Horne GCM, Abburi Venkata K, Pirling T. The effects of residual stress on elastic-plastic fracture propagation and stability. Mater Des 2018;143:131–40. http://dx.doi.org/10.1016/j.matdes.2018.01.064.

[18] Withers PJ. Residual stress and its role in failure. Rep Progr Phys 2007;7(12):2211. http://dx.doi.org/10.1088/0034-4885/70/12/R04.

[19] Farrahi GH, Lebrijn JL, Couratin D. Effect of shot peening on residual stress and fatigue life of a spring steel. Fatigue Fract Eng Mater Struct 1995;18(2):211–20. http://dx.doi.org/10.1111/j.1460-2695.1995.tb00156.x.

[20] Anderson TL. Fracture mechanics: Fundamentals and applications. 3rd ed. CRC Press; 2005, p. 451–507.

[21] M'Saoubi R, Axinte D, Soo SL, Nobel C, Attia H, Kappmeyer G, et al. High performance cutting of advanced aerospace alloys and composite materials. CIRP Ann Manuf Technol 2015;64(2):557–80. http://dx.doi.org/10.1016/j.cirp.2015.05.002.

[22] Weston N, Thomas B, Jackson M. Processing metal powders via field assisted sintering technology (FAST): A critical review. Mater Sci Technol 2019;35:1306–28. http://dx.doi.org/10.1080/02670836.2019.1620538.

[23] Levano Blanch O, Lunt D, Baxter GJ, Jackson M. Deformation behaviour of a FAST diffusion bond processed from dissimilar titanium alloy powders. Metall Mater Trans A 2021;52(7):3064–82. http://dx.doi.org/10.1007/s11661-021-06301-w.

[24] ASTM International. ASTM E8/E8M-16 - Standard Test Methods for Tension Testing of Metallic Materials. Tech. rep., 2016, p. 1–29. http://dx.doi.org/10.1520/E0008-E0008M-16.

[25] Vock S, Klöden B, Kirchner A, Weißgärber T, Kieback B. Powders for powder bed fusion: A review. Prog Addit Manuf 2019. http://dx.doi.org/10.1007/s40964-019-00078-6.

[26] Malekipour E, El-Mounayri H. Common defects and contributing parameters in powder bed fusion AM process and their classification for online monitoring and control: A review. Int J Adv Manuf Technol 2018;95:1–4. http://dx.doi.org/10.1007/s00170-017-1172-6.

[27] Weston N, Derguti F, Tudball A, Jackson M. Spark plasma sintering of commercial and development titanium alloy powders. J Mater Sci 2015;50:4860–78. http://dx.doi.org/10.1007/s10853-015-9029-6.

[28] Seco Tools. Online cutting data suggestion tool: SMG S12 - face milling. 2021, URL https://www.secotools.com/dashboard/Suggest/Suggest.

[29] Oosthuizen GA, Akdogan G. The performance of PCD tools in high-speed milling of Ti6Al4V. Int J Adv Manuf Technol 2011;52:929–35. http://dx.doi.org/10.1007/s00170-010-2804-2.

[30] Li A, Zhao J, Wang D, Zhao J. Failure mechanisms of a PCD tool in high-speed face milling of Ti-6Al-4V alloy. Int J Adv Manuf Technol 2013;67:1959–66. http://dx.doi.org/10.1007/s00170-012-4622-1.

[31] Childerhouse T, Hernández-Nava E, Tapoglou N, M'Saoubi R, Franca L, Leahy W, et al. The influence of finish machining depth and hot isostatic pressing on defect distribution and fatigue behaviour of selective electron beam melted Ti-6Al-4V. Int J Fatigue 2021;147:106169. http://dx.doi.org/10.1016/j.ijfatigue.2021.106169.

[32] Bantounas I, Lindley TC, Rugg D, Dye D. Effect of microtexture on fatigue cracking in Ti–6Al–4V. Acta Mater 2007;55(16):5655–65. http://dx.doi.org/10.1016/j.actamat.2007.06.034.

[33] Dunne FPE, Rugg D. On the mechanisms of fatigue facet nucleation in titanium alloys. Fatigue Fract Eng Mater Struct 2008;31(11):949–58. http://dx.doi.org/10.1111/j.1460-2695.2008.01284.x.

[34] Pilchak AL, Williams JC. Observations of facet formation in near-α titanium and comments on the role of hydrogen. Metall Mater Trans A 2011;42(4):1000–27. http://dx.doi.org/10.1007/s11661-010-0507-9.

[35] Jackson M, Boyer RR. Titanium and its alloys: Processing, fabrication and mechanical performance. In: Encyclopedia of aerospace engineering. John Wiley & Sons, Ltd; 2010, http://dx.doi.org/10.1002/9780470686652.eae199.

[36] Shen Q, Zhanqiang L, Hua Y, Zhao J, Lv W, Mohsan AUH. Effects of cutting edge microgeometry on residual stress in orthogonal cutting of Inconel 718 by FEM. Materials 2018;11:1015. http://dx.doi.org/10.3390/ma11061015.

[37] Li A, Pang J, Zhao J, Zang J, Wang F. FEM-simulation of machining induced surface plastic deformation and microstructural texture evolution of Ti-6Al-4V alloy. Int J Mech Sci 2017;123:214–23. http://dx.doi.org/10.1016/j.ijmecsci.2017.02.014.

[38] Bergengren Y, Larsson M, Melander A. The influence of machining defects and inclusions on the fatigue of a hardened spring steel. Fatigue Fract Eng Mater Struct 1995;18:1071–87. http://dx.doi.org/10.1111/j.1460-2695.1995.tb00840.x.